

# The CT10 NNLO Global Analysis of QCD

Jun Gao,<sup>1</sup> Marco Guzzi,<sup>2</sup> Joey Huston,<sup>3</sup> Hung-Liang Lai,<sup>4</sup> Zhao Li,<sup>5</sup>  
Pavel Nadolsky,<sup>1</sup> Jon Pumplin,<sup>3</sup> Daniel Stump,<sup>3</sup> and C.-P. Yuan<sup>3,6</sup>

<sup>1</sup> *Department of Physics, Southern Methodist University, Dallas, TX 75275-0181, USA*

<sup>2</sup> *Deutsches Elektronensynchrotron DESY,  
Notkestrasse 85 D-22607 Hamburg, Germany*

<sup>3</sup> *Department of Physics and Astronomy,  
Michigan State University, East Lansing, MI 48824-1116, USA*

<sup>4</sup> *Taipei Municipal University of Education, Taipei, Taiwan*

<sup>5</sup> *Institute of High Energy Physics,  
Chinese Academy of Sciences, Beijing 100049, China*

<sup>6</sup> *Center for High Energy Physics, Peking University, Beijing 100871, China*

## Abstract

We present next-to-next-to-leading order (NNLO) parton distribution functions (PDFs) from the CTEQ-TEA group. The CT10NNLO PDF fit is based on essentially the same global data sets used in the CT10 and CT10W NLO PDF analyses. After exploring the goodness of the fits to the HERA combined data and the Tevatron jet data, we present various predictions at NNLO accuracy for both existing and forthcoming precision measurements from the CERN Large Hadron Collider. The range of variations in the gluon distribution introduced by correlated systematic effects in inclusive jet production is also examined.

PACS numbers: 12.15.Ji, 12.38 Cy, 13.85.Qk

Keywords: parton distribution functions; electroweak physics at the Large Hadron Collider

## Contents

<b>I. Introduction</b>	3
<b>II. Heavy-flavor scheme in the CT10NNLO fit</b>	4
A. QCD factorization for heavy quarks in the S-ACOT- $\chi$ scheme	4
B. The S-ACOT- $\chi$ scheme at NNLO in a nutshell	6
C. A phenomenological illustration	8
<b>III. Global analysis with correlated systematic errors</b>	8
A. Log-likelihood function in the CT10 NNLO analysis	10
B. PDF eigenvector sets and $\alpha_s$ uncertainty	12
C. Implementation of correlated systematic errors	13
<b>IV. Experimental data sets and theoretical updates</b>	14
<b>V. The CT10NNLO parton distribution functions</b>	16
<b>VI. Comparisons to individual experiments</b>	21
A. Deep-inelastic scattering at HERA	22
B. W charge asymmetry and vector boson production	24
C. Inclusive jet production from Run-2 at the Tevatron	24
D. Correlated systematic errors in Tevatron jet production	26
<b>VII. Collider phenomenological predictions</b>	32
A. W and Z total cross sections	33
B. Top quark pair production, total cross sections	34
C. W and Z rapidity distributions	35
D. ATLAS inclusive jet distribution	39
E. SM Higgs boson total cross sections	41
<b>VIII. Discussion and Conclusion</b>	41
<b>Acknowledgments</b>	42
<b>References</b>	42

## I. INTRODUCTION

A global analysis of perturbative QCD makes use of experimental data from many short-distance scattering processes to construct, within some approximation, universal parton distribution functions (PDFs) for the proton. These PDFs can be used to calculate hadronic cross sections. The CTEQ global analysis at the next-to-leading order (NLO) in the strong coupling constant  $\alpha_s$  has been developed over decades. Examples of general-purpose PDFs in this series include CTEQ6, published in 2002 [1], followed by CTEQ6.1 in 2003 [2]. Starting from CTEQ6.5 published in 2006 [3], and in ensuing PDF sets such as CTEQ6.6 [4] and CT09 [5], the effects of finite quark masses on the CTEQ global analysis have been implemented in the S-ACOT- $\chi$  factorization scheme [6–9] at NLO accuracy. The most recent CTEQ NLO PDFs, named CT10 and CT10W, were published in 2010 [10] and are currently in wide use in phenomenological predictions for the Tevatron, LHC, and other experiments.

The data from the CERN Large Hadron Collider (LHC) cover a wide kinematic range with high expected precision; a similar level of precision is needed for the theoretical predictions. Thus, there is a need for using cross sections calculated up to next-to-next-to-leading order (NNLO) in the strong coupling constant  $\alpha_s$  with parton distribution function sets that are also determined at NNLO. Complete calculations for this order in  $\alpha_s$  are available for the running coupling  $\alpha_s(Q)$ , PDF evolution in  $Q$  [11, 12], matrix elements in deep-inelastic scattering (DIS) [13–19], and vector boson production [20, 21]. NNLO matrix elements are unknown for several other processes in the global analysis. Most notably, the key input theoretical cross section for inclusive jet production in  $pp^{(-)}$  collisions is still evaluated at NLO, although some of the NNLO radiative contributions have been already computed [22, 23].<sup>1</sup> Various NNLO PDF sets have been published in the literature [24–29] that make use of NNLO matrix elements when available.

In this paper, we present a new generation of CTEQ parton distributions, at NNLO, named CT10 NNLO.<sup>2</sup> They are obtained from a global analysis of QCD data in which three changes have been made to include the calculations at NNLO. First, the parton distribution functions  $f(x, Q)$  are evolved according to the 3-loop Dokshitzer-Gribov-Lipatov-Altarelli-Parisi (DGLAP) equations. Second, the strong coupling  $\alpha_s(\mu_R)$  evolves in the renormalization scale  $\mu_R$  according to the 3-loop beta function. Third, the hard matrix elements for DIS and vector boson production are calculated up to two QCD loops. A detailed implementation of neutral-current DIS cross sections in the S-ACOT- $\chi$  scheme, which performs a consistent treatment of non-zero masses of heavy partons, up to this order of accuracy is documented in Ref. [31] and recapped in Sec. II.

The experimental data sets included in the CT10NNLO fit are essentially the same as in the CT10 and CT10W NLO fits, with the exceptions of Tevatron Run-1 inclusive jet data and a subset of the Tevatron Run-2 lepton charged asymmetry data from  $W$  boson decays.

---

<sup>1</sup> Some other cross sections, such as for Higgs boson production and diboson production, have been calculated to NNLO, but to date have not been implemented in any global analysis.

<sup>2</sup> Parametrizations of the CT10NNLO PDFs were publicly released in 2012 [30].

The changes in the selection of the experimental data sets are summarized in Sec. IV. No LHC data are included in the CT10 NNLO analysis, which can therefore be used to make predictions based exclusively on the pre-LHC data. [The impact of the LHC data will be investigated in the post-CT10 fits.]

As stated previously, the inclusive jet cross sections in the CT10NNLO analysis are still evaluated with NLO matrix elements, hence require special scrutiny. The experimental data on the inclusive jet cross sections are statistically very precise but have significant systematic uncertainties. We examine variations in the gluon and other PDFs caused by the QCD scale dependence and by various treatments of systematic uncertainties in inclusive jet production. The impact of jet-related uncertainties is compared to those from other sources.

For consistency with the CT10 NLO PDFs, CT10 NNLO assumes the same value of the QCD coupling strength  $\alpha_s(M_Z) = 0.118$  and pole masses for heavy quarks of  $m_c = 1.3$  GeV and  $m_b = 4.75$  GeV. The CT10NNLO eigenvector PDF sets are available on the CTEQ web site [32], and in the LHAPDF standard format [33]. Together with the PDF eigenvector sets for the central value of  $\alpha_s(M_Z) = 0.118$ , an additional PDF series in which  $\alpha_s(M_Z)$  is varied in the range 0.112-0.127 are provided. These PDFs are sufficient for computing the correlated PDF+ $\alpha_s$  uncertainty by adding the PDF and  $\alpha_s$  uncertainties in quadrature, as explained in Ref. [34].

The outline of the paper is as follows. Section II reviews our NNLO implementation of DIS cross sections, placing an emphasis on the treatment of heavy-quark contributions. Section III summarizes the statistical procedure of the global analysis, most notably the definition of the log-likelihood function and the implementation of correlated systematic errors. Section IV lists the experimental data used in the CT10NNLO analysis. Section V describes some features of the resulting CT10NNLO PDFs, while Section VI presents detailed comparisons of data and theory. Section VII presents NNLO predictions for collider measurements based on the CT10NNLO PDFs, and Section VIII contains our summary and conclusions.

## II. HEAVY-FLAVOR SCHEME IN THE CT10NNLO FIT

### A. QCD factorization for heavy quarks in the S-ACOT- $\chi$ scheme

A consistent implementation of contributions from the massive quarks ( $c$  and  $b$ ) is a prerequisite and challenge for a viable NNLO PDF analysis. The mass dependence of the heavy-quark DIS contributions to PDF fits affects QCD precision observables in a wide range of energies [3]. Heavy-quark mass effects were studied in PDF fits since mid-1990's in the context of several theoretical approaches, or “heavy-quark schemes”. The S-ACOT- $\chi$  factorization scheme [6–9] has been adopted in the recent NLO fits CTEQ6HQ [35], 6.5 [3], 6.6 [4], and CT10 [10]. For the present work, the S-ACOT- $\chi$  scheme has been extended to

NNLO accuracy, *i.e.*,  $\mathcal{O}(\alpha_s^2)$ , in the computation of neutral-current DIS cross sections [31].<sup>3</sup> The alternative TR' scheme [36, 37] is used in the MSTW and HERAPDF fits, while the FONLL scheme [38, 39] has been adopted by the NNPDF collaboration. The BMSN scheme [40, 41] and the fixed-flavor number (FFN) schemes are used by the ABM and GJR groups, respectively.

The general-mass variable flavor number (GM-VFN) schemes replace the zero-mass approximation, which is no longer adequate for describing the DIS data. They evaluate the coefficient functions using the exact dependence on heavy-quark mass  $m_h$ , while heavy-quark PDFs provide an approximation for collinear production of  $h\bar{h}$  pairs when  $Q^2 \gg m_h^2$ . They are valid across the whole range of  $Q$  values accessed in the global fits.<sup>4</sup>

Less variation in the predictions of various heavy-quark schemes was observed when going from NLO to NNLO calculations [31, 44]. For example, the spread of theoretical predictions for the standard-candle  $W$  and  $Z$  boson production cross sections at the LHC has shrunk from 6-8% at NLO [4] (with the largest deviations observed with the zero-mass PDFs) to 2-3% at NNLO [45–47]. Quark-mass effects continue to be important. Their non-equivalent treatment by various PDF analysis groups gives rise to residual uncertainties in the standard candle predictions and in the observables sensitive to the gluon or heavy-quark scattering, such as Higgs boson production.

The NNLO calculation in the S-ACOT- $\chi$  scheme in Ref. [31] focused on two issues that had not been earlier addressed. First, we clarified the connection of the GM-VFN scheme at NNLO to the proof of QCD factorization for DIS with massive quarks presented by Collins [7]. It was demonstrated that the S-ACOT- $\chi$  scheme can be derived to all orders from Collins' approach and is validated by a QCD factorization theorem.

Second, we documented an algorithm that organizes the NNLO S-ACOT- $\chi$  calculation in close analogy to the zero-mass VFN computation. As a result, the NNLO DIS cross sections can be constructed step-by-step from components that can be found in literature. In the S-ACOT- $\chi$  scheme, all elements arise from the all-order factorization formalism, which is not always the case in other frameworks. These features distinguish the S-ACOT- $\chi$  scheme from the TR' and FONLL schemes that follow different implementation approaches.

As a result, the structure of the S-ACOT- $\chi$  cross sections is readily reproducible; the universality of the PDFs follows from the Collins proof of QCD factorization [31]. The  $Q$  dependence of the QCD coupling and PDFs is found by numerical QCD evolution that assumes one shared  $N_f$  value in each  $Q$  range; QCD quantities for  $N_f$  and  $N_f + 1$  active flavors are related at the switching energy scales through the matching conditions. The NNLO radiative contributions are assembled straightforwardly from the matrix elements in the massive FFN [17–19] and zero-mass VFN schemes [13–16], as well as from the mass-dependent operator matrix elements for the heavy-quark PDFs [40].

---

<sup>3</sup> The charged-current DIS cross sections, for which some  $\mathcal{O}(\alpha_s^2)$  massive amplitudes are not available, are evaluated at NLO.

<sup>4</sup> A complementary approach (an intermediate-mass scheme) uses approximate quark mass dependence in all scattering channels [42]. DIS cross sections in this approach utilizing the exact  $\mathcal{O}(\alpha_s)$  massive ACOT terms and approximate  $\mathcal{O}(\alpha_s^2)$  and  $\mathcal{O}(\alpha_s^3)$  massive terms have been recently published [43].

The S-ACOT- $\chi$  scheme reduces to the FFN scheme at the heavy-quark threshold  $Q^2 \approx m_h^2$  and to the zero-mass  $\overline{MS}$  scheme at  $Q^2 \gg m_h^2$ , without additional renormalization. The matching of the GM-VFN cross sections to the FFN cross sections near the mass threshold is generally not automatic. To realize it, the TR' and FONLL scheme introduce additional elements (constraints on the  $Q$  dependence of the heavy-quark DIS contributions in the TR' scheme and the “damping factor” in the FONLL framework) that are not stipulated by the QCD factorization theorem. In the S-ACOT- $\chi$  scheme, threshold matching is rather a consequence of the energy conservation condition that suppresses the difference between the GM-VFN and FFN results when  $Q^2$  approaches  $m_h^2$ . This is achieved by restricting the allowed form for the approximate coefficient functions that describe QCD scattering off an initial-state heavy quark, so that they comply with energy conservation. It leads to the effective rescaling ( $\chi$  rescaling) of the light-cone momentum fraction in the approximate heavy-quark scattering terms [9, 48].

The derivation of mass-dependent contributions from the QCD factorization theorem, which is shown to be compatible with the rescaled terms, leads to more confident constraints on the PDFs. Our fitting code implements these NNLO Wilson coefficient functions in the S-ACOT- $\chi$  scheme together with the HOPPET program for the evolution of  $\alpha_s$  and PDFs [49], in which the switching points between the active flavors can be expressed either in terms of the  $\overline{MS}$  masses or pole masses.<sup>5</sup> The fitting program can read either the pole masses or  $\overline{MS}$  masses as an input. If the  $\overline{MS}$  masses are selected as the input, they are converted into the pole masses when needed, *e.g.*, to evaluate those operator matrix elements  $A_{ab}^{(2)}$  that are published in terms of the pole masses. In the CT10 NNLO fit, the pole masses  $m_c = 1.3$  GeV and  $m_b = 4.75$  GeV have been assumed.

## B. The S-ACOT- $\chi$ scheme at NNLO in a nutshell

In the S-ACOT- $\chi$  scheme, a generic *inclusive* structure function  $F_{2,L} \equiv F$  takes form of a convolution product ( $\otimes$ ) of the Wilson coefficient functions  $C_{ia}$  and the parton distribution functions  $f_{a/p}(\xi, \mu)$ :

$$\begin{aligned} F(x, Q) &= \sum_{i=1}^{N_f^{fs}} e_i^2 \sum_{a=0}^{N_f} \int_x^1 \frac{d\xi}{\xi} C_{ia} \left( \frac{x}{\xi}, \frac{Q}{\mu}, \frac{m_h}{\mu}, \alpha_s(\mu) \right) f_{a/p}(\xi, \mu) \\ &\equiv \sum_{i=1}^{N_f^{fs}} e_i^2 \sum_{a=0}^{N_f} [C_{ia} \otimes f_{a/p}] (x, Q), \end{aligned} \quad (1)$$

where  $\xi$  is the light-cone momentum fraction,  $\mu$  is the factorization scale,  $N_f$  indicates the number of active flavors, and  $N_f^{fs}$  is the number of the produced final-state flavors (most

---

<sup>5</sup> The authors want to thank Gavin Salam for his help with the setup of this code.

generally,  $N_f^{fs} \neq N_f$ ). The structure function can be also written as

$$F = \sum_{l=1}^{N_l} F_l + \sum_{h=N_{l+1}}^{N_f^{fs}} F_h, \quad (2)$$

where  $l$  and  $h$  are the indices of light-quark and heavy-quark flavors probed to the photon, respectively [39]. [Note that the S-ACOT- $\chi$  scheme can simultaneously account for several flavors with non-zero masses]. On the right-hand side,

$$F_l = e_l^2 \sum_a [C_{l,a} \otimes f_{a/p}] (x, Q), \quad F_h = e_h^2 \sum_a [C_{h,a} \otimes f_{a/p}] (x, Q). \quad (3)$$

The  $\mathcal{O}(\alpha_s^2)$  radiative contributions,  $F_l^{(2)}$  and  $F_h^{(2)}$ , are

$$F_l^{(2)} = e_l^2 \left\{ C_{l,l}^{NS,(2)} \otimes (f_{l/p} + f_{\bar{l}/p}) + c^{PS,(2)} \otimes \Sigma + c_{l,g}^{(2)} \otimes f_{g/p} \right\}, \quad (4)$$

$$F_h^{(2)} = e_h^2 \left\{ c_{h,h}^{NS,(2)} \otimes (f_{h/p} + f_{\bar{h}/p}) + C_{h,l}^{(2)} \otimes \Sigma + C_{h,g}^{(2)} \otimes f_{g/p} \right\}, \quad (5)$$

where the lower-case notation  $c_{a,b}^{(2)}$  indicates a zero-mass Wilson coefficient function, the uppercase notation  $C_{a,b}^{(2)}$  indicates a massive coefficient function, and  $\Sigma(x, \mu) = \sum_{i=1}^{N_f} [f_{i/p}(x, \mu) + f_{\bar{i}/p}(x, \mu)]$  denotes the singlet-quark PDF. These equations have the same form as the factorized expressions for the zero-mass structure functions. Their components are listed explicitly in Ref. [31]. In this derivation, we employ a rescaling convention [9] to construct the LO, NLO, and NNLO coefficient functions with initial-state heavy quarks,  $c_{a,h}^{(k)}$  with  $k = 0, 1$ , and 2, and the associated subtraction terms. They are obtained by evaluating the zero-mass expressions as a function of the rescaling variable  $\chi$ :

$$c_{l,h}^{(k)} \left( \frac{x}{\xi}, \frac{Q}{\mu}, \frac{m_h}{Q} \right) = c_{h,h}^{(k)} \left( \frac{\chi}{\xi}, \frac{Q}{\mu}, m_h = 0 \right) \theta(\chi \leq \xi \leq 1), \quad (6)$$

where

$$\chi = x \left( 1 + \frac{(\sum_{fs} m_h)^2}{Q^2} \right), \quad (7)$$

and  $\sum_{fs} m_h$  is the sum of the heavy-quark masses in the final state (equal to  $2m_h$  in the lowest-order  $c\bar{c}$  pair production). These rescaled coefficient functions obey energy conservation and vanish near the production threshold, so that the FFN result is reproduced in this limit.

Eqs. (4) and (5) apply to the inclusive DIS functions  $F_2$ ,  $F_L$ , etc. In the case of semi-inclusive DIS production of heavy quarks, the definition of the semi-inclusive (SI) structure functions  $F_{h,SI}$ , such as  $F_2^{c\bar{c}}$  measured at HERA, requires additional care in order to obtain infrared-safe results at all  $Q$  [41]. In the CT10NNLO global fit, the following approximation for  $F_{h,SI}$  has been adopted [31, 39]. At moderate  $Q$  values accessible at HERA, it is defined as

$$F_{h,SI}^{(2)}(x, Q) = F_h^{(2)}(x, Q) + \sum_{l=1}^{N_l} e_l^2 L_{l,q}^{NS,(2)} \otimes (f_{l/p} + f_{\bar{l}/p}), \quad (8)$$



where  $F_h^{(2)}(x, Q)$  is the  $\mathcal{O}(\alpha_s^2)$  contribution to the inclusive DIS function  $F(x, Q)$  arising from photon scattering on a heavy quark, cf. Eq. (5). The function  $L_{I,q}^{NS,(2)}(\xi, Q/\mu, m_h/\mu)$  is the non-singlet part of the light-quark component  $F_l(x, Q)$  that contains radiation of a  $h\bar{h}$  pair in the final state, computed in Ref. [19]. In the kinematic region  $Q < 10$  GeV, which supports most of the HERA charm production data, we observe that  $L_{I,q}^{NS,(2)}$  contributes about 0-3% on the semi-inclusive charm cross section, *i.e.*, it is small compared to the typical experimental errors.

### C. A phenomenological illustration

In Fig. 1, the CT10 NLO/NNLO predictions for  $F_2^{c\bar{c}}$  are compared to a recent data set from the H1 collaboration [50], in which the charm structure function  $F_2^{c\bar{c}}$  was extracted from the  $D^*$  meson distribution. Predictions for  $F_2^{c\bar{c}}$  are computed as a function of the momentum fraction  $x$  for five different bins of  $Q$ . The dashed red lines and solid blue lines represent the S-ACOT- $\chi$  predictions at NLO and NNLO, respectively. The inputs are the pole mass  $m_c = 1.3$  GeV and the strong coupling constant  $\alpha_s(M_Z) = 0.118$ . Although this specific data set [50] was not included in the CT10 fits, the overall agreement is very good. The NLO and NNLO predictions are close to one another for the most part, at least in the intermediate  $10^{-3} \leq x \leq 10^{-2}$  kinematic region, in which the bulk of the data was collected. However, the NLO prediction is shown for a particular factorization scale that improved agreement with the data,  $\mu = \sqrt{Q^2 + m_c^2}$ , while a more typical scale choice  $\mu = Q$  was taken at NNLO. In general, the NLO predictions for  $F_2^{c\bar{c}}$  are characterized by a wide band of the scale dependence uncertainty. This band is reduced significantly when going to NNLO, and the NNLO predictions in the S-ACOT- $\chi$  scheme are closer to those in the FONLL-C and TR' schemes [31]. The NNLO predictions are therefore more robust compared to NLO.

## III. GLOBAL ANALYSIS WITH CORRELATED SYSTEMATIC ERRORS

For completeness, and in order to establish notations for the ensuing discussion, in this section we summarize the statistical procedure adopted in the CT10NNLO analysis. An important aspect of this procedure is to determine the *uncertainties* of the PDFs, which arise from several sources, both experimental and theoretical.

Experimental uncertainties may be uncorrelated between different measurements, such as the bin-by-bin *statistical error* on the measured cross section. Some experimental uncertainties are highly correlated between different measurements within one experiment or even among several experiments. The *luminosity error* is an example of a correlated experimental uncertainty in a data set. It affects equally the normalization of all cross section measurements from the experiment. Other correlated uncertainties typically exist and may have impact that is comparable to the luminosity error.

Inclusion of the correlated experimental errors utilizing their standard deviations pub-



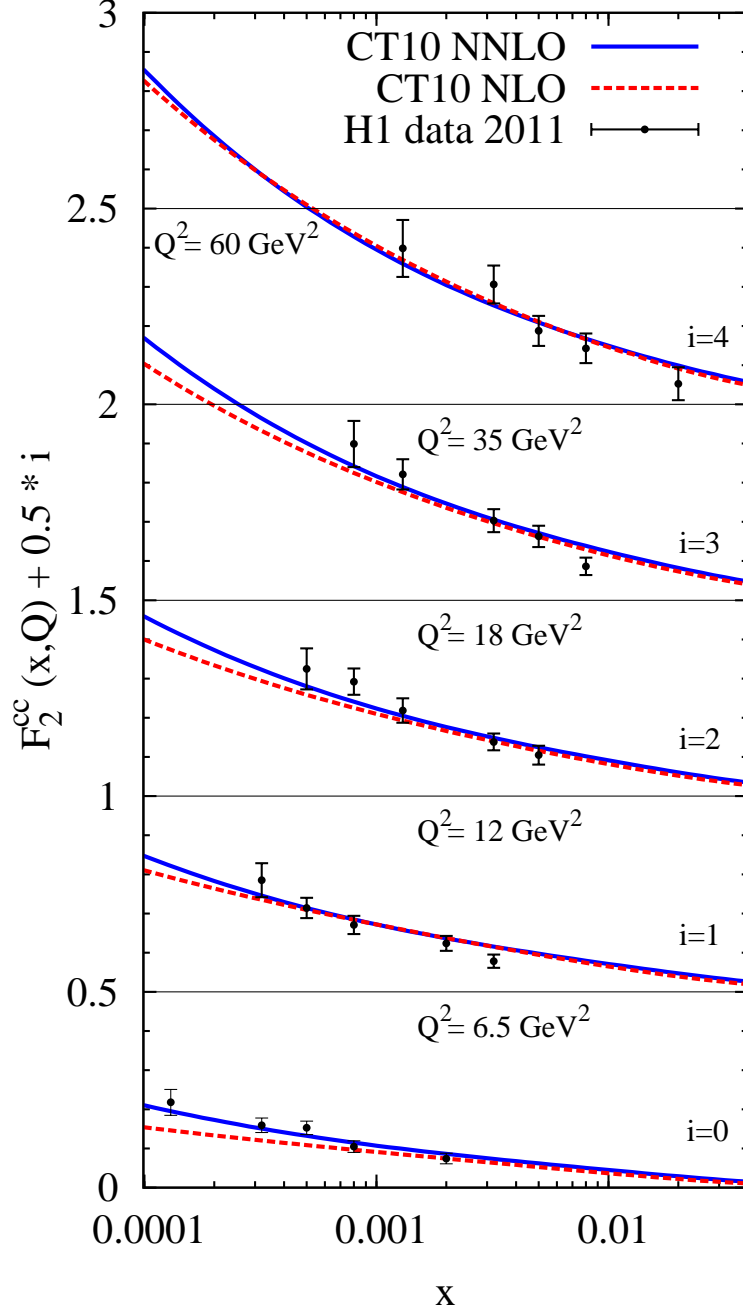


FIG. 1: The semi-inclusive heavy-quark function  $F_2^{c\bar{c}}$  as a function of  $x$  in different bins of  $Q$ . The CT10NLO, CT10NNLO predictions and H1 data [50] are compared.

lished by the experiments began in the CTEQ program with the construction of the CTEQ6 parton distributions [1]. This is achieved by constructing an appropriate figure-of-merit function  $\chi^2$  that includes errors from both uncorrelated and correlated sources, as shown explicitly in Sec. III A.

By examining the  $\chi^2$  function in the neighborhood of the best fit and its dependence

on  $\alpha_s$ , the CT10 global analysis determines a family of independent eigenvector sets that can be used to propagate the combined PDF+ $\alpha_s$  uncertainty into theoretical predictions (cf. Sec. III B). The central PDF set and PDF eigenvector sets are generally sensitive to the implementation of correlated systematic errors in the fit. Possible procedures for reconstructing the correlation error matrix from the published standard deviations, and the expected modifications in the PDFs that they induce, are discussed in Sec. III C. A numerical comparison of these procedures will be presented in Sec. VI.

### A. Log-likelihood function in the CT10 NNLO analysis

A typical experiment  $E$  in the global fit publishes a set of measurements  $\{M_i; i = 1, 2, 3, \dots, N_{pt}\}$ , consisting of a central value  $D_i$  for the observable, a standard deviation for the *uncorrelated* experimental error  $s_i$ , and standard deviations  $\beta_{k\alpha}$  for each of  $N_\alpha$  systematic errors, where  $k = 1, 2, 3, \dots, N_\alpha$ . We do not know the experimental errors, but experiments provide their standard deviations. So we write

$$D_i = X_i + s_i \delta_i + \sum_{\alpha=1}^{N_\alpha} \beta_{k\alpha} \lambda_\alpha \quad (9)$$

where  $X_i$  is the “true” value of the observable.<sup>6</sup> Equation (9) defines *nuisance parameters*,  $\delta_i$  and  $\lambda_\alpha$ . These will be random numbers with mean value 0 and standard deviation 1,

$$\langle \delta_i \rangle = 0 \text{ and } \langle \delta_i^2 \rangle = 1; \quad (10)$$

$$\langle \lambda_\alpha \rangle = 0 \text{ and } \langle \lambda_\alpha^2 \rangle = 1. \quad (11)$$

We assume that the uncorrelated errors are completely uncorrelated among the  $N$  measurements; that is,

$$\langle \delta_i \delta_j \rangle = \delta_{ij}. \quad (12)$$

We also assume that the systematic errors are completely correlated among the  $N_{pt}$  measurements; that is,  $\lambda_\alpha$  does not depend on  $i$ . However, the systematic errors are among themselves uncorrelated,

$$\langle \lambda_\alpha \lambda_\beta \rangle = \delta_{\alpha\beta}. \quad (13)$$

The goal of the global analysis is to find the theoretical parameters for which the theoretical values  $T_i$  of the observables are as close as possible to the “true” values,  $X_i$ . In Eq. (9) replace  $X_i$  by  $T_i$ . Then we are led to minimize the differences, by defining

$$\chi_E^2(\{a\}, \{\lambda\}) = \chi_D^2 + \chi_\lambda^2, \quad (14)$$

where

$$\chi_D^2 \equiv \sum_{k=1}^{N_{pt}} \frac{1}{s_k^2} \left( D_k - T_k - \sum_{\alpha=1}^{N_\lambda} \beta_{k,\alpha} \lambda_\alpha \right)^2, \quad (15)$$

---

<sup>6</sup> The “true” value is the *mean value* of  $D_i$  that would result from a large number of independent experiments.

and

$$\chi_\lambda^2 \equiv \sum_{\alpha=1}^{N_\lambda} \lambda_\alpha^2, \quad (16)$$

and minimizing  $\chi_E^2$  with respect to the theory parameters. However, there are additional sources of systematic uncertainties associated with the unknown nuisance parameters  $\{\lambda_\alpha\}$ . Therefore, to have agreement between theory and data within the standard deviations of the experimental errors, we also vary the  $\{\lambda_\alpha\}$  values, seeking to make  $\chi_E^2$  small.

Because  $\chi_E^2$  is only a quadratic function of  $\{\lambda_\alpha\}$ , we may obtain the minimum of  $\chi_E^2$  with respect to  $\{\lambda_\alpha\}$  analytically [51]. At the minimum, the nuisance parameters take the values

$$\bar{\lambda}_\alpha = \sum_{i=1}^{N_{pt}} \frac{D_i - T_i}{s_i} \sum_{\delta=1}^{N_\lambda} \mathcal{A}_{\alpha\delta}^{-1} \frac{\beta_{i,\delta}}{s_i}, \quad (17)$$

where

$$\mathcal{A}_{\alpha\beta} = \delta_{\alpha\beta} + \sum_{k=1}^{N_{pt}} \frac{\beta_{k,\alpha} \beta_{k,\beta}}{s_k^2}. \quad (18)$$

The corresponding best-fit representation for  $\chi_E^2$  is

$$\min \chi_E^2 = \sum_{i,j}^{N_{pt}} (D_i - T_i) (\text{cov}^{-1})_{ij} (D_j - T_j). \quad (19)$$

It includes the inverse of the covariance matrix

$$(\text{cov})_{ij} \equiv s_i^2 \delta_{ij} + \sum_{\alpha=1}^{N_\lambda} \beta_{i,\alpha} \beta_{j,\alpha}, \quad (20)$$

given by

$$(\text{cov}^{-1})_{ij} = \left[ \frac{\delta_{ij}}{s_i^2} - \sum_{\alpha,\beta=1}^{N_\lambda} \frac{\beta_{i,\alpha}}{s_i^2} \mathcal{A}_{\alpha\beta}^{-1} \frac{\beta_{j,\beta}}{s_j^2} \right]. \quad (21)$$

The best-fit value of  $\chi_D^2$  can be also expressed in terms of the data  $D_{sh,i}$  that are “shifted” from the central values by the best-fit correlated errors,

$$\min \chi_D^2 = \sum_{i=1}^{N_{pt}} (D_{sh,i} - T_i)^2 / s_i^2; \quad (22)$$

Here

$$D_{sh,i} = D_i - \sum_{\alpha=1}^{N_\alpha} \beta_{i\alpha} \bar{\lambda}_\alpha. \quad (23)$$

we quote the function  $\min \chi_D^2$  in Table I as a useful measure of the agreement between theory and data for each experiment. In Sec. VI, we will also use  $\chi_E^2 = \chi_D^2 + \chi_\lambda^2$  as another measure of the agreement between theory and data.

Thus far, we have considered only a single experiment. The *global* chi-square function that is minimized in the CT10 global analysis sums over all experiments  $E$  and includes a contribution  $\chi_{th}^2(\{a\})$  specifying theoretical conditions for the PDF parameters:

$$\chi_{\text{global}}^2 = \sum_E \chi_E^2 + \chi_{th}^2. \quad (24)$$

The function  $\chi_{th}^2$  is introduced to prevent some unconstrained PDF parameters from reaching values that might lead to unphysical predictions at small Bjorken  $x$  (specifically,  $x \leq 10^{-4}$ ), where experimental constraints are sparse [4]. It rules out those PDF parameter combinations that may result in negative cross sections or unlikely flavor dependence. The specific condition imposed in the CT10 analysis is to constrain the ratio  $R_s(x, Q) = [s(x, Q) + \bar{s}(x, Q)] / [\bar{u}(x, Q) + \bar{d}(x, Q)]$  of the strange PDFs to non-strange sea PDFs to be in the interval  $0.5 \leq R_s(x, Q_0) \leq 1.5$  at the initial scale  $Q_0$  and  $x$  below  $10^{-5}$ . In the current fit, the  $R_s$  ratio is not constrained in this region by the experimental data, hence a loose theory-motivated constraint needs to be imposed.

The global  $\chi^2$  function in Eq. (24) is constructed by assuming that both uncorrelated and correlated errors are quasi-Gaussian and symmetric. When an experiment provides asymmetric errors, we symmetrize them. The exact procedure for symmetrization of errors has low impact on the outcome of the fit, as the number of points with very asymmetric errors typically is small compared to the total number of points and parameters.

## B. PDF eigenvector sets and $\alpha_s$ uncertainty

Besides the central (best-fit) PDF set, the CT10NNLO release includes PDF eigenvector sets to estimate the uncertainty range of our PDF fits using the Hessian method [51, 52] and either the symmetric [1] or asymmetric [10, 53] master formula to estimate the PDF uncertainties. The Hessian method is based on an iterative procedure for finding linear combinations of the fitting parameters by diagonalization of the Hessian matrix. In the CT10NNLO fit, we use 25 free parameters to describe the parton distributions at  $Q_0$ , and hence have 25 eigenvector directions. For each of these directions, we find a pair of eigenvector sets defined by moving away from the best-fit location (where  $\chi^2$  takes its minimum value) by a distance that estimates the boundary of the 90% confidence interval for each experiment.

The method to find these eigenvectors is explained in [10]. In addition to including an upper “tolerance” bound on the increase in total  $\chi^2$  that realizes the 90% c.l. agreement on average, as in the CTEQ6 analysis, we include a penalty term in  $\chi^2$  that quickly grows when the PDF set fails to describe any specific experiment. The effective function  $\chi_{Eff}^2$  that is constructed this way is scanned along each eigenvector direction until  $\chi_{Eff}^2$  increases above the tolerance bound or quick  $\chi_{Eff}^2$  growth due to the penalty is triggered.

The penalty term is constructed from statistical variables  $S$  derived from  $\chi_E^2$  values for individual experiments [10]. In contrast to  $\chi_E^2$ , the variables  $S$  obey an approximate standard normal distribution independently of  $N_{pt}$ , which simplifies the comparison of confidence

levels between data sets containing widely different numbers of points. The quasi-Gaussian  $S$  variables are found by using a simpler Fisher’s approximation [54] in the CT10 NLO fit (reliable for experiments with many data points,  $N_{pt} \gtrsim 9$ ) and more accurate Lewis’ approximation [55] in the CT10NNLO analysis.

We note that even in the central fit, some data sets have  $\chi_E^2/N_{pt}$  that lie outside the 90 % confidence level. That is not surprising, of course, since there are 28 data sets—naively the chance for all of them to lie with 90 % confidence is only  $0.9^{28} = 0.05$ . To allow for this, for each data set that has  $\chi_E^2 > N_{pt}$  in the central fit, we rescale its  $\chi_E^2$  by a factor  $N_{pt}/\chi_{central\,fit}^2$  before computing the penalty.

In practical applications, the PDF uncertainty obtained with the Hessian eigenvector sets must be combined with the  $\alpha_s$  uncertainty. The procedure for combining these uncertainties is described in [34]. The central and error eigenvector sets of the CT10NNLO family assume  $\alpha_s(M_Z) = 0.118$ , which is compatible with the world-average value. In addition we provide best-fit PDF sets for other  $\alpha_s(M_Z)$  values in the interval 0.112-0.127. For a theory observable, the 90% c.l.  $\alpha_s$  uncertainty can be estimated from the difference of predictions using PDF sets with  $\alpha_s = 0.116$  and 0.120. Then, the PDF+ $\alpha_s$  uncertainty with all correlations can be estimated by adding the PDF and  $\alpha_s$  uncertainties in quadrature.

### C. Implementation of correlated systematic errors

In the treatment of correlated systematic errors, there is another subtlety concerned with the distinction between additive and multiplicative systematic uncertainties. The correlated systematic errors fall into two classes: additive errors, for which the experiment can determine the absolute value  $\beta_{i,\alpha}$  of the standard deviation; or multiplicative errors, for which only the relative fraction  $\sigma_{i,\alpha} = \beta_{i,\alpha}/X_i$  is known. The two kinds must be handled differently to avoid a bias in the outcome of the fit. However, it is a common practice in many experiments to publish the correlated systematic uncertainties as the relative percentage errors  $\sigma_{i,\alpha}$  regardless of whether the systematic error is additive or multiplicative, rather than the absolute values  $\beta_{i,\alpha}$ .

To reconstruct the correlation matrix as

$$\beta_{i,\alpha} = \sigma_{i,\alpha} X_i, \tag{25}$$

one selects the reference central value  $X_i$  for each datum. Since the additive errors are supposedly independent of the theory predictions, it is natural, although not necessary, to use the experimental central values  $D_i$  as the references,  $\beta_{i,\alpha} = \sigma_{i,\alpha} D_i$ .

For a multiplicative error, the reference to  $D_i$  is generally unacceptable, as random fluctuations in  $D_i$  tend to bias the best-fit parameters. A well-known multiplicative bias described by D’Agostini arises in the treatment of the normalization of the data [56, 57]. A fit that references the normalization error to  $D_i$  would underestimate the true cross section. This downward bias is prevented if smoothly behaving  $X_i$  values are used as the references, such as the theoretical values  $T_i$  at each data point ( $\beta_{i,\alpha} = \sigma_{i,\alpha} T_i$ ).

Most of the time the experimental paper does not distinguish between the additive and multiplicative errors. In this case, the global fit has to choose between several ways, and several tradeoffs, for computing  $\beta_{i,\alpha}$ . When preparing the CT10 NNLO PDFs, we explored various procedures for the computation of  $\beta_{i,\alpha}$  that have been identified in recent literature. [See also a related discussion in the appendix of Ref. [58].]

1. Method  $D$ , or the “experimental normalization” method, normalizes *all correlated errors* to the experimental central values: that is, we compute  $\beta_{i,\alpha} = \sigma_{i,\alpha} D_i$ , for all additive and multiplicative errors alike. In this method, the correlated errors are independent of theory predictions. However, they are affected by irregular fluctuations of the central data points, which may result in a pronounced D’Agostini bias in the best-fit parameters when the fluctuations are large.
2. Method  $T$  normalizes the *multiplicative errors* to the theoretical values that are updated in every fitting iteration. “The  $T^{(0)}$  method” [59] is a variation on this approach in which the multiplicative errors are updated once in many iterations. The  $T^{(0)}$  method was proposed to prevent nonlinear behavior of  $\chi^2$  that may occur in method  $T$ . *Additive errors* in these methods remain normalized to  $D_i$ . Both methods  $T$  and  $T^{(0)}$  are free of D’Agostini’s bias, as the multiplicative errors are estimated by using a smooth function. Method  $T^{(0)}$  converges to the true solution after several updates of the  $T_i^{(0)}$  values, provided the partial derivatives  $\partial\chi^2/\partial T_i^{(0)}$  are negligible, and may fail to do so otherwise. Our comparisons follow the original implementation of the  $T$  and  $T^{(0)}$  methods [59], in which only the luminosity errors (but not other multiplicative errors such as for the jet energy scale) were referenced to  $T_i$  ( $T_i^{(0)}$ ).
3. An extended version of method  $T$  normalizes *both additive and multiplicative errors* to the current theoretical values,  $\beta_{i,\alpha} = \sigma_{i,\alpha} T_i$ . Similarly, the extended method  $T^{(0)}$  normalizes all correlated errors to fixed theoretical values,  $\beta_{i,\alpha} = \sigma_{i,\alpha} T_i^{(0)}$ . The advantage of these methods is that  $\beta_{i,\alpha}$  shows the smoothest behavior among all considered.

The extended method  $T$  is used by default in our NLO fits. At NNLO the implementation of systematic effects became even more important, given the reduction in other uncertainties. In Sec. VID we compare five procedures for implementation of systematic errors in inclusive jet production, where the systematic effects are among the most pronounced. We use the extended  $T$  method for other scattering processes.

#### IV. EXPERIMENTAL DATA SETS AND THEORETICAL UPDATES

The experimental data sets included in the CT10 NNLO fit are listed in Table I. With a small number of exceptions, they were chosen to be the same as in the CT10 NLO fit. At NLO, we presented two PDF sets, designated as CT10 and CT10W. The distinction between them concerns the inclusion of the DØ Run-2 data for the rapidity asymmetry ( $A_\ell$ ) of the charged lepton from  $W$  boson decay. This data was included in the CT10W analysis, with an extra weight, but not included in the CT10 analysis. More specifically, the CT10W analysis

includes the  $A_\ell$  data points in three ranges of the lepton transverse momentum ( $p_{T\ell}$ ) in the electron decay channel, and one  $p_{T\ell}$  bin in the muon decay channel. After the publication of the CT10 and CT10W analyses, the DØ collaboration has recommended not to include those two less inclusive data sets in  $p_{T\ell}$ , *i.e.*, with  $25 \leq p_{T\ell} \leq 35$  GeV and  $p_{T\ell} \geq 35$  GeV. In the CT10NNLO analysis, only the most inclusive data with  $p_{T\ell} \geq 25$  GeV, in both the electron and muon decay channels, are included in the analysis. Since CT10NNLO includes only a part of the DØ  $A_\ell$  data that distinguishes between CT10 and CT10W PDFs, it can be treated as an NNLO counterpart to either the CT10 or CT10W NLO PDF sets.

The Tevatron Run-2 inclusive jet data have a wider rapidity coverage (in the case of CDF) and smaller statistical and systematic errors, as compared to the Tevatron Run-1 data. Their effects on the global analysis have been extensively discussed in Ref. [5]. We concluded that since the Run-1 jet data are not perfectly consistent with the Run-2 data sets, one may ask if the Run-1 jet contributions should be retained. In the CT10NNLO analysis, we do not include the Tevatron Run-1 inclusive jet data. This choice has implications for the large- $x$  gluon PDF, as will be shown later.

The data selection choices in regard to the Tevatron  $W$  asymmetry and inclusive jet production affect mainly certain combinations of the PDFs at  $x > 0.1$ : specifically the ratio  $d/u$  (down- versus up-quark PDFs) and the gluon PDF. These combinations change by amounts that are mostly comparable to the PDF uncertainties obtained in the NLO analysis.

Besides implementing the NNLO QCD contributions in neutral-current DIS and vector boson production, we updated the theoretical treatment of several experiments. In the coefficient functions for deep inelastic scattering, we have updated the definitions of the electroweak couplings describing  $Z$  and  $\gamma^* - Z$  interference contributions. This update mildly modifies the  $d$  quark PDFs at large  $x$ .

In the previous global analyses, the NLO jet cross sections were using tabulated point-by-point ratios of NLO/LO cross sections ( $K$  factors) computed with the EKS code [85]. The original EKS calculation was published in the 1990's and had limited accuracy when comparing it to the latest precision jet data. A deeply modified version of the EKS code (MEKS) was prepared to provide advanced predictions for jet cross sections [86]. The MEKS calculation is entirely independent from NLOJET++ [87], another frequently used program for computation of NLO jet cross sections. A comparison to MEKS validated predictions from FASTNLO [88–90] and APPLGRID [91], the interfaces for fast interpolation of NLO-JET++ cross sections. The specific input settings for which the MEKS, FASTNLO, and APPLGRID programs agree to a few percent were documented [58, 86]. The magnitude of theoretical uncertainties in inclusive jet cross sections was also estimated. It was observed, for example, that the current NLO QCD scale dependence is too large at the highest  $P_{Tj}$  and  $y_j$  of the LHC inclusive jet data set to provide meaningful constraints on the relevant PDFs. This situation is expected to be improved when the NNLO inclusive jet cross section calculation becomes available.

In the CT10NNLO fit, we compute the NLO inclusive jet cross sections with FASTNLO version 1.0 and cross-validate the results using MEKS. The two-loop threshold correction [92] was not included. In the jet cross sections, both the factorization and renormalization



Experimental data set	$N_{pt}$	CT10NNLO	CT10W
Combined HERA1 NC and CC DIS [60]	579	1.07	1.17
BCDMS $F_2^p$ [61]	339	1.16	1.14
BCDMS $F_2^d$ [62]	251	1.16	1.12
NMC $F_2^p$ [63]	201	1.66	1.71
NMC $F_2^d/F_2^p$ [63]	123	1.23	1.28
CDHSW $F_2^p$ [64]	85	0.83	0.66
CDHSW $F_3^p$ [64]	96	0.81	0.75
CCFR $F_2^p$ [65]	69	0.98	1.02
CCFR $xF_3^p$ [66]	86	0.40	0.59
NuTeV neutrino dimuon SIDIS [67]	38	0.78	0.94
NuTeV antineutrino dimuon SIDIS [67]	33	0.86	0.91
CCFR neutrino dimuon SIDIS [68]	40	1.20	1.25
CCFR antineutrino dimuon SIDIS [68]	38	0.70	0.78
H1 $F_2^c$ [69]	8	1.17	1.26
H1 $\sigma_r^c$ for $c\bar{c}$ [70, 71]	10	1.63	1.54
ZEUS $F_2^c$ [72]	18	0.74	0.90
ZEUS $F_2^c$ [73]	27	0.62	0.76
E605 Drell-Yan process, $\sigma(pA)$ [74]	119	0.80	0.81
E866 Drell Yan process, $\sigma(pd)/(2\sigma(pp))$ [75]	15	0.65	0.64
E866 Drell-Yan process, $\sigma(pp)$ [76]	184	1.27	1.21
CDF Run-1 $W$ charge asymmetry [77]	11	1.22	1.24
CDF Run-2 $W$ charge asymmetry [78]	11	1.04	1.02
DØ Run-2 $W \rightarrow e\nu_e$ charge asymmetry [79]	12	2.17	2.11
DØ Run-2 $W \rightarrow \mu\nu_\mu$ charge asymmetry [80]	9	1.65	1.49
DØ Run-2 $Z$ rapidity distribution [81]	28	0.56	0.54
CDF Run-2 $Z$ rapidity distribution [82]	29	1.60	1.44
CDF Run-2 inclusive jet production [83]	72	1.42	1.55
DØ Run-2 inclusive jet production [84]	110	1.04	1.13
<b>Total:</b>	<b>2641</b>	<b>1.11</b>	<b>1.13</b>

TABLE I: Experimental data sets examined in the CT10NNLO and CT10W NLO analyses, together with their  $\chi^2$  values.

scales are chosen to be equal to the transverse momentum  $P_{Tj}$  of each individual jet. This choice is different from the one adopted in the CTEQ6.X and CT10 NLO analyses, where both scales were set to  $P_{Tj}/2$ .

## V. THE CT10NNLO PARTON DISTRIBUTION FUNCTIONS

With a similar setup as in the CT10/CT10W NLO analysis, the CT10NNLO fit results in about the same quality of the fit expressed in terms of the total chi-square. We obtain  $\chi^2$  of order 2950 for 2641 data points, with minor variations dependent on the setup of the

fit. In the rest of the paper, we discuss representative results from the new fit, assuming NNLO PDFs, unless stated otherwise.

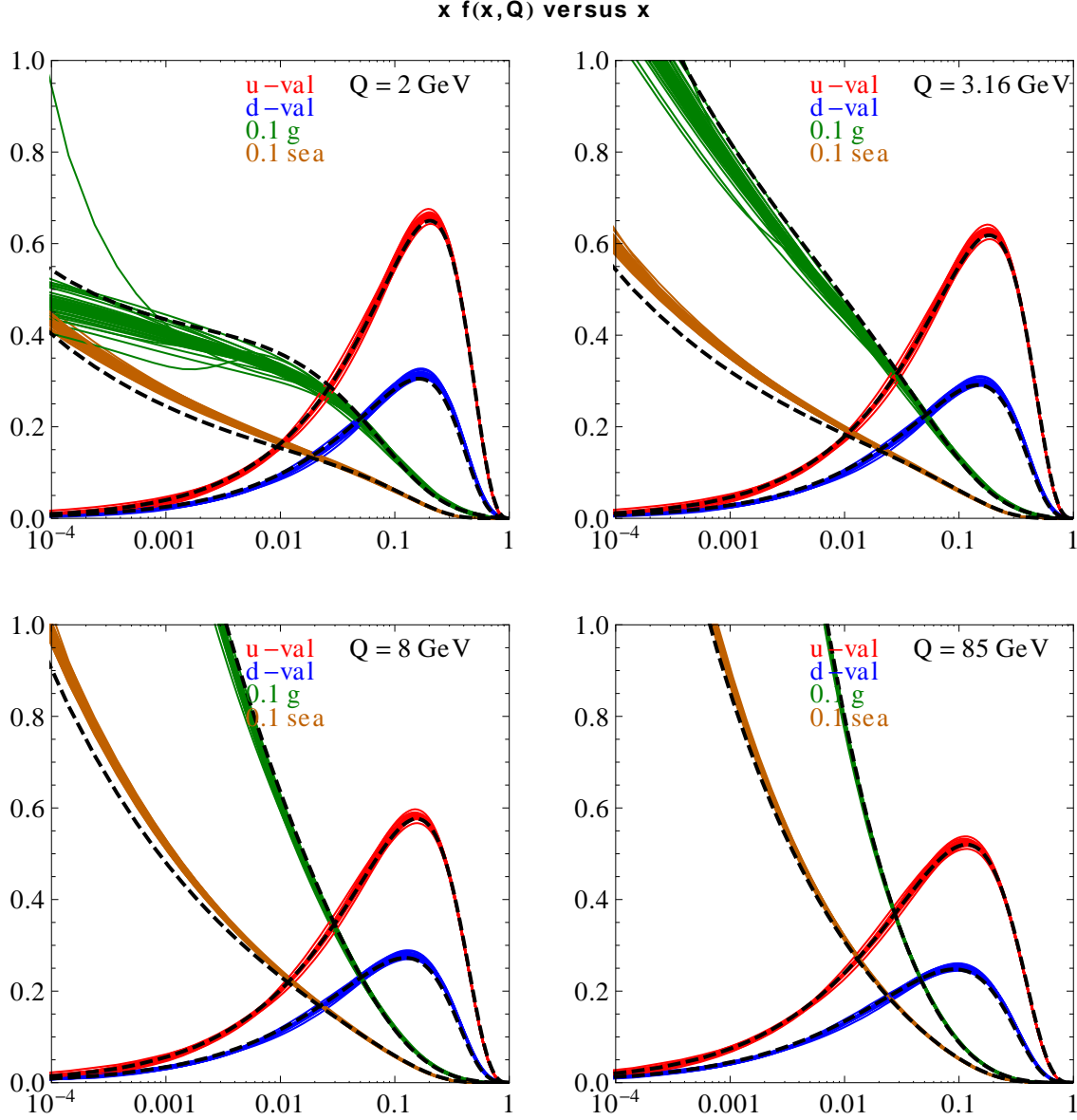


FIG. 2: CT10NNLO parton distribution functions. These figures show the Hessian error PDFs from the CT10NNLO analysis. Each graph shows  $x u_{\text{valence}} = x(u - \bar{u})$ ,  $x d_{\text{valence}} = x(d - \bar{d})$ ,  $0.10 x g$  and  $0.10 x q_{\text{sea}} = 2(\bar{d} + \bar{u} + \bar{s})$  as functions of  $x$  for a fixed value of  $Q$ . The values of  $Q$  are 2, 3.16, 8, 85 GeV. The quark sea contribution is  $q_{\text{sea}} = 2(\bar{d} + \bar{u} + \bar{s})$ . The dashed curves are the central CT10 NLO fit.

The central fit and PDF eigenvector sets are shown in Fig. 2. In addition to obtaining the *central fit*, there is also a need to understand the uncertainty ranges of the PDFs, resulting from the experimental uncertainties of the data included in the fit. For this purpose, we generate 50 alternate fits using the Hessian method. Figure 2 indicates the PDFs for the alternate fits, also called the “error PDFs”, in addition to the central fit. In each graph,

PDFs for 4 parton combinations are shown, by plotting  $xf(x, Q)$  versus  $x$  for a fixed value of  $Q$ . The parton combinations are  $f = u_{\text{valence}}, d_{\text{valence}}, g, q_{\text{sea}}$ . The values of  $Q$  are 2, 3.16, 8, 85 GeV. The dashed curves are the corresponding functions for the CT10 NLO PDFs. Those can differ by significant amounts from the NNLO ones in some regions of the  $(x, Q)$  space, especially where  $x$  and  $Q$  are small.

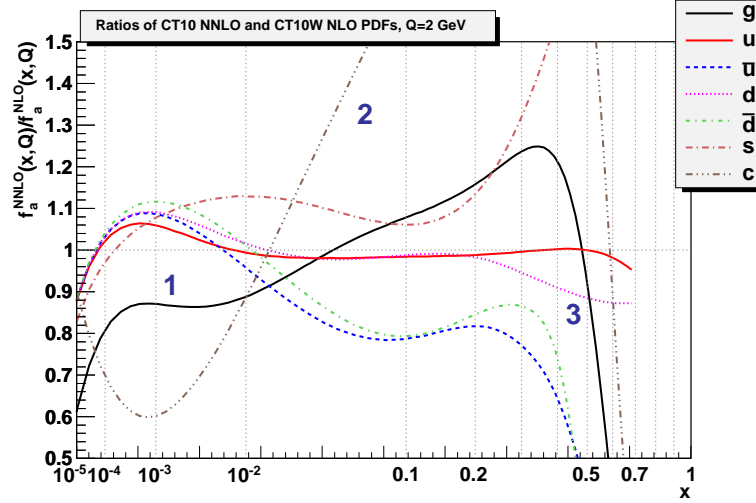


FIG. 3: Ratios of various CT10NNLO central fit parton distributions to those of the CT10W central fit, at  $Q = 2$  GeV.

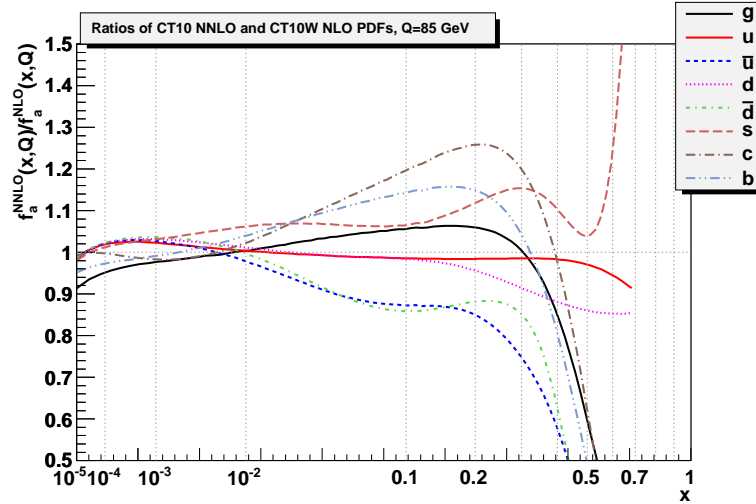


FIG. 4: Same as Fig. 3, at  $Q = 85$  GeV.

To better assess these differences, Fig. 3 shows the ratios of various parton distributions from the CT10NNLO central fit to those from the CT10W NLO central fit, at  $Q = 2$  GeV. A few changes are noticeable: (1) At  $x < 10^{-2}$ , the  $\mathcal{O}(\alpha_s^2)$  evolution in CT10NNLO suppresses  $g(x, Q)$  and increases  $q(x, Q)$ , as compared to CT10W PDFs. (2) The heavy charm  $c(x, Q)$  and bottom  $b(x, Q)$  partons change as a result of adopting the  $\mathcal{O}(\alpha_s^2)$  GM VFN scheme in

the CT10NNLO analysis. (3) In the large- $x$  region,  $g(x, Q)$  and  $d(x, Q)$  are reduced by the removal of the Tevatron Run-1 inclusive jet data, the revised electroweak couplings, the alternative treatment of correlated systematic errors, and the scale choices.

A similar comparison, but for  $Q = 85$  GeV, is shown in Fig. 4. It also indicates that at  $x > 0.1$ ,  $d(x, Q)$ ,  $\bar{u}(x, Q)$  and  $\bar{d}(x, Q)$  are all reduced in CT10NNLO, compared to CT10W. Likewise,  $g(x, Q)$  is also reduced in the large  $x$  region.

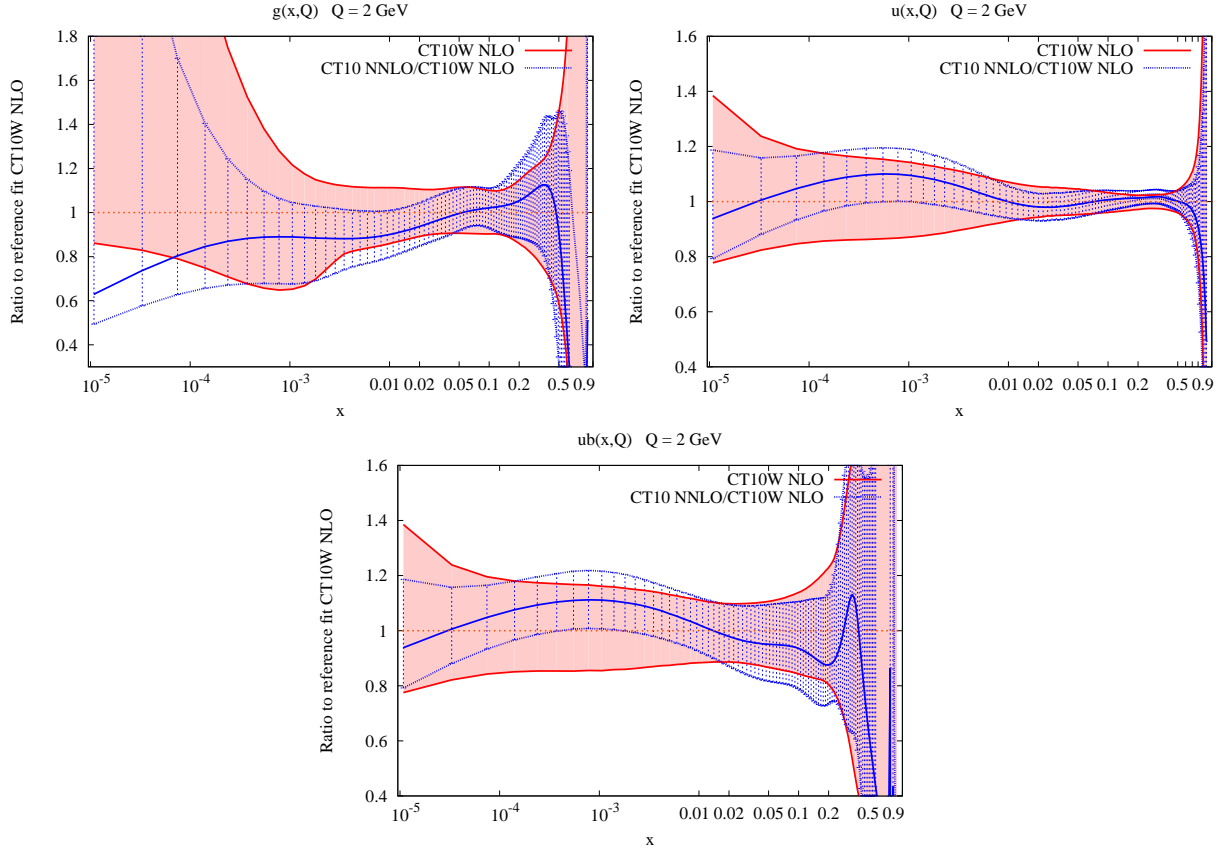


FIG. 5: Comparison of CT10NNLO error PDFs to CT10W (NLO) error PDFs. All are expressed as ratios to the central fit of the CT10W set.

The uncertainties of CT10NNLO PDFs for various parton flavors are shown in Figure 5, compared to the CT10W (NLO) uncertainties, at  $Q = 2$  GeV.

The CT10NNLO central fit is compared to that of MSTW2008NNLO [24] in Figure 6. It shows that the CT10NNLO gluon and quarks are larger as  $x \rightarrow 0$ . At the smallest  $x$  values and at the initial scale  $Q_0$ , the CT10 NNLO gluon remains positive, although consistent with zero, as a result of the chosen form of parametrization. We also note that CT10NNLO strangeness is larger at  $x \sim 10^{-3}$ .

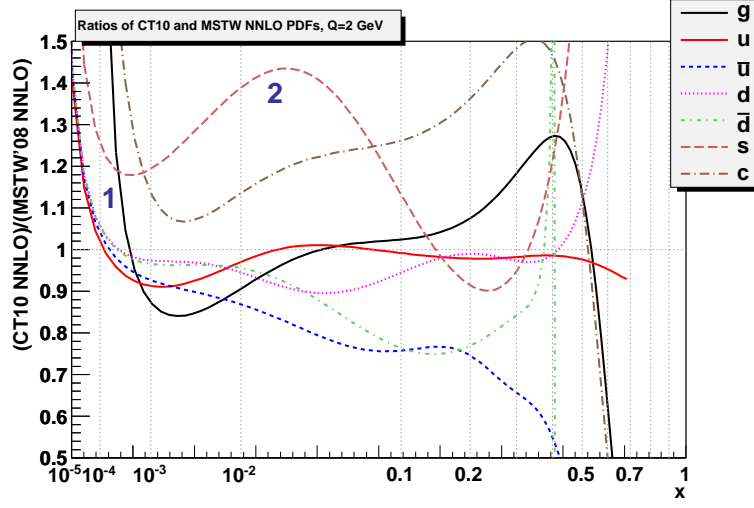


FIG. 6: Ratios of various CT10NNLO central fit parton distributions to those of the MSTW2008NNLO central fit, at  $Q = 2 \text{ GeV}$ .

## VI. COMPARISONS TO INDIVIDUAL EXPERIMENTS

As was already observed, the goodness of the NNLO fit to most experiments is about the same as for CT10(W) NLO, and the changes in going to the NNLO analysis are comparable to the experimental uncertainties. The differences in  $\chi^2_E$  rarely exceed the expected statistical fluctuations of order  $\sqrt{2N_{pt}}$ . Some improvement is observed in the fit to the HERA-1 combined data on DIS, the Tevatron Run-2 jet production data, and the CCFR and NuTeV dimuon SIDIS. In this section, we present examples of the description of the data by the CT10 theoretical predictions, focusing on select precise measurements in DIS,  $W$  boson production, and jet production.

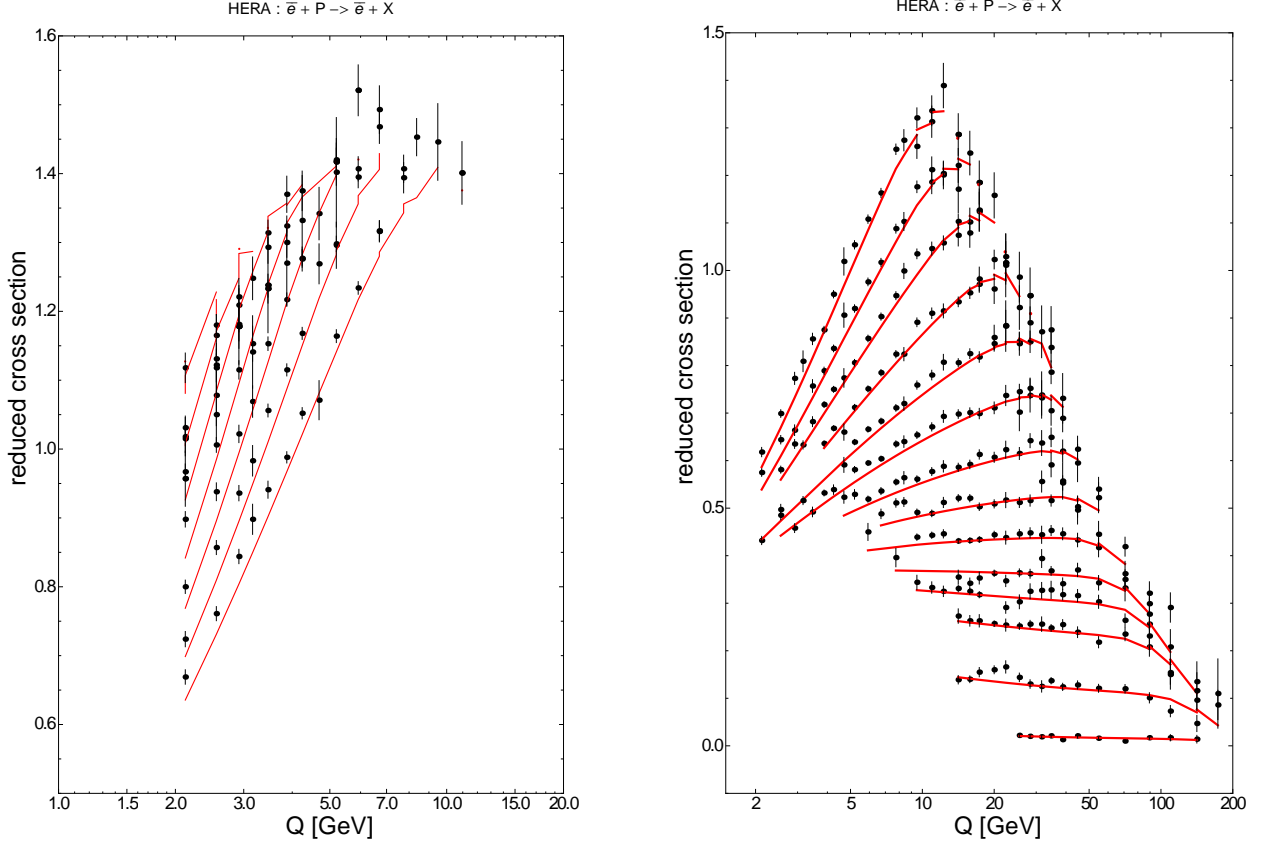


FIG. 7: The HERA combined data, with comparison to theory. The reduced cross section  $\sigma_r(x, Q)$  for NC DIS of positrons is plotted as a function of  $Q$  for 33 values of  $x$ . The graph on the left has  $x$  values in the range  $0 < x < 0.002$ ; the one on the right has  $0.002 \leq x \leq 0.65$ . The points are the published central values, while error bars correspond to the uncorrelated errors only. The red curves show the theoretical value of the reduced cross section  $\sigma_r(x, Q)$  computed with CT10NNLO PDFs.

### A. Deep-inelastic scattering at HERA

The HERA combined data set for  $e^+p$  neutral current (NC) and charged current (CC) deep-inelastic scattering [60] has 579 measurements of the reduced cross section  $\sigma_r(x, Q)$ , after applying our restrictions  $Q \geq 2$  GeV and  $W \geq 3.5$  GeV, where the invariant mass of the hadronic final state is  $W = Q\sqrt{1/x - 1}$ .

In Fig. 7 we show the  $e^+p$  NC DIS reduced cross sections (366 data points) along with their *uncorrelated* error bars. Data are divided into two blocks: small  $x$  is shown on the left, *i.e.*,  $0 < x < 0.002$ , and large  $x$  is shown on the right, *i.e.*,  $0.002 \leq x \leq 0.65$ . Fig. 7 also shows theory curves based on the CT10NNLO parton distribution functions, superimposed on the the HERA combined data. Note that there are systematic differences between the central data and the theory, as there should be due to the systematic uncertainties of the data. Our detailed comparison of data and theory must indicate whether the systematic differences are consistent with the published errors [29].

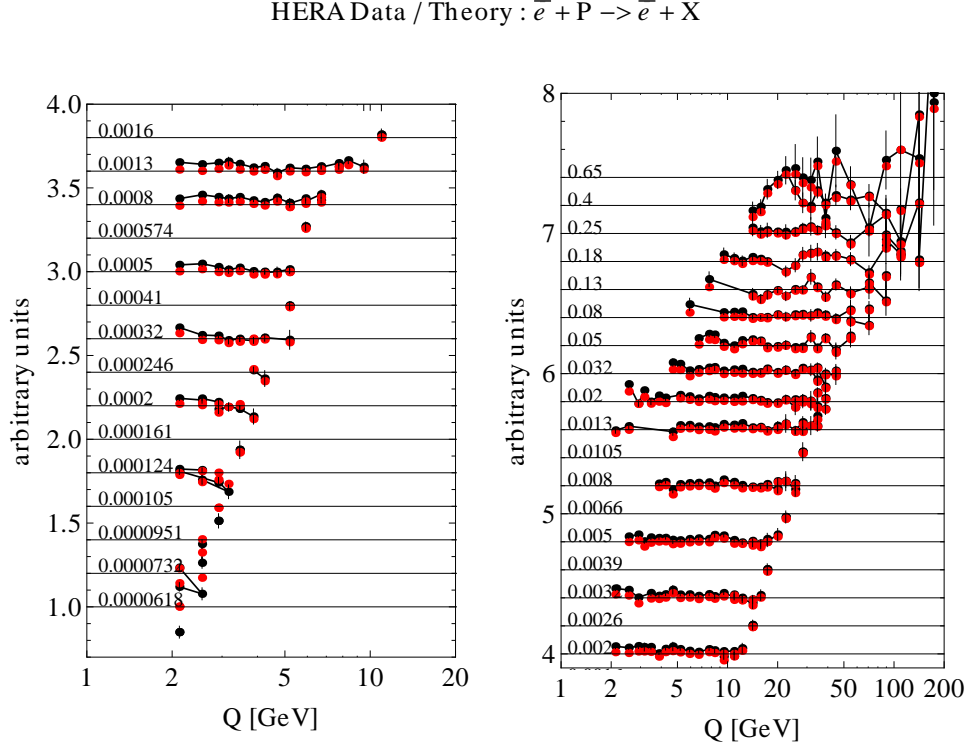


FIG. 8: Ratio of data divided by theory, for the reduced cross section for positron-proton NC DIS. Theory is represented by the horizontal lines. Indicated in both figures are the  $x$ -values:  $0 < x \leq 0.0016$  in the left inset;  $0.002 \leq x \leq 0.65$  in the right inset. Black dots are experimental central values with uncorrelated errors only. Red dots are the optimally shifted data, where the shifts are evaluated according to the Hessian analysis of the systematic errors.

Data divided by theory for  $e^+p$  NC DIS is shown in Figure 8, in which we have a clearer illustration of the differences. The horizontal lines are marked by the corresponding values



of  $x$ . The black dots are the central experimental values, shown along with uncorrelated error bars. The red dots are the optimally shifted data values, determined by the Hessian analysis. We observe that the systematic shifts bring data and theory into better agreement, as expected.

A histogram of the residuals of the shifted data, defined by

$$\text{Residual}_i = \left( D_i - \sum_{\alpha=1}^{N_\lambda} \beta_{i\alpha} \bar{\lambda}_\alpha - T_i \right) / s_i \equiv (D_{sh,i} - T_i) / s_i, \quad (26)$$

is shown in Figure 9. The  $i$ -th residual is defined by the difference between the optimally shifted data and the theory, normalized to the uncorrelated error. The total number of systematic errors is  $N_\lambda = 114$ . The curve shown in Fig. 9 is the standard normal distribution, with no adjustable parameters: it has a mean = 0, standard deviation = 1, and integral = 1. The close similarity between the histogram of residuals and the Gaussian curve implies that the data and theory agree within the experimental errors, and that the experimental errors have been correctly estimated.

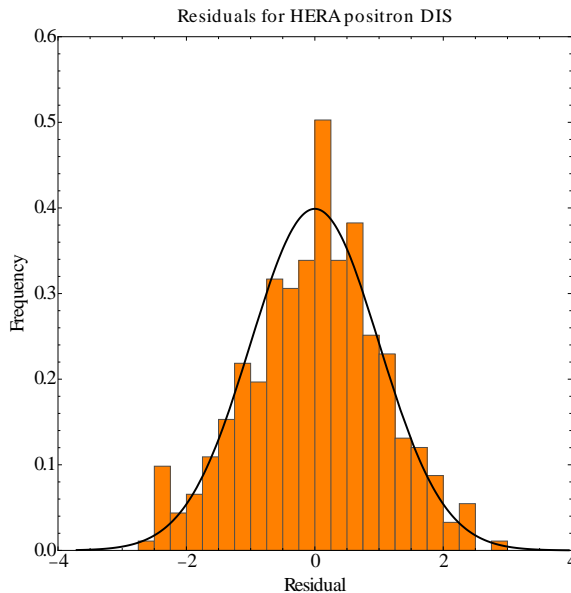


FIG. 9: Histogram of residuals for the HERA combined data for positron-proton NC DIS. The residuals are defined in Eq. (26). The solid curve is the standard normal distribution, for comparison.

The best-fit nuisance parameters  $\{\bar{\lambda}_\alpha\}$  for the HERA data are shown in the histogram of Figure 10. The fact that the histogram agrees with the standard normal distribution shows that theory matches data within expectations based on the published correlated systematic errors.

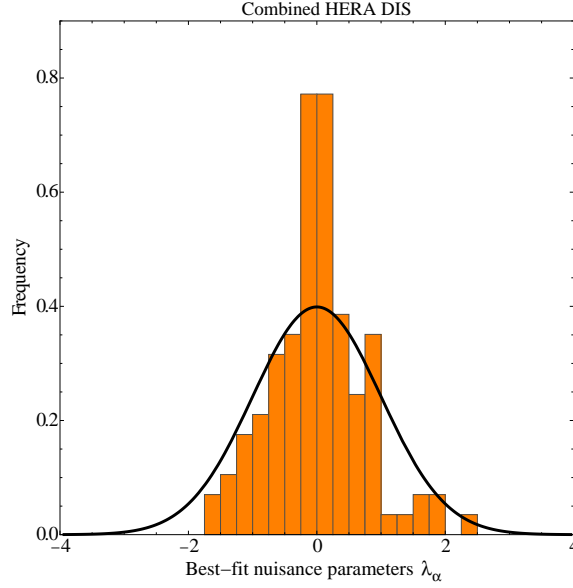


FIG. 10: Histogram of the optimal normalized shift variables  $\{\bar{\lambda}_\alpha\}$  for the HERA combined data. There are 114 systematic errors, all of which apply to all of the 579 measurements in the HERA combined data set. The solid curve the standard normal distribution, for comparison.

### B. $W$ charge asymmetry and vector boson production

The  $W$  charge asymmetry measured at the Tevatron is primarily sensitive to the shape of the ratio  $d(x, M_W)/u(x, M_W)$  at  $x$  values above 0.1. The NNLO fit produces essentially the same quality of the agreement with the included Tevatron  $W$  asymmetry sets as the CT10W NLO PDF set. The  $\chi^2/N_{pt}$  values for these data sets are listed in Table I. As an illustration, Fig. 11 shows the CT10W NLO and CT10 NNLO data residuals for the 12 points of the D0 Run-2 lepton asymmetry data in the electron [79] and muon [80] decay channels. The residuals are very close for the two PDF sets. The quality of the NLO and NNLO fits to other data sets on vector boson production is also comparable.

### C. Inclusive jet production from Run-2 at the Tevatron

The CT10NNLO global analysis only includes the Tevatron Run-2 inclusive jet data for the reasons explained in Sec. IV. In what follows we examine the goodness of CT10NNLO fits to the Run-2 inclusive jet data.

In Fig. 12 we show the differential cross section  $d^2\sigma/(dy_j dP_{Tj})$  for inclusive jet production at DØ Tevatron Run-2 [84]. The various curves correspond to the six rapidity intervals  $0 - 0.4$ ,  $0.4 - 0.8$ ,  $0.8 - 1.2$ ,  $1.2 - 1.6$ ,  $1.6 - 2.0$ , and  $2.0 - 2.4$ . The points are the central data values, while the error bars (too small to be seen in most cases) represent uncorrelated errors. In the same figure, we also show the theory calculations based on the CT10NNLO parton

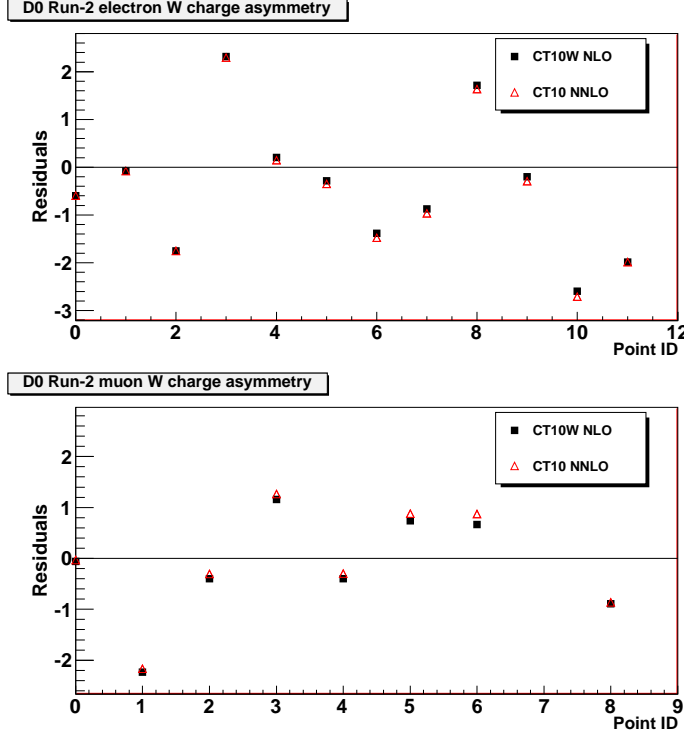


FIG. 11: Point-by-point residuals for the DØ Run-2 charge asymmetry data in the electron (upper inset) and muon (lower inset) channels. The residuals are defined in Eq. (26).

distribution functions. In this figure we do not show systematic errors. With the systematic shifts, we obtain  $\chi^2_E/N_{pt} = 115/110$  for DØ Run-2, where 15 units are contributed by the penalty term  $\chi^2_\lambda$  for the 23 nuisance parameters ( $\lambda_\alpha$ ) controlling the systematic shifts, cf. the definition in Eq. (14). The overall effect of the correlated systematic shifts is significant, compared to the small uncorrelated errors, and is of the same order as in the CT10 NLO fits. More detailed comparisons, illustrating the impact of the systematic shifts on the jet data at NLO, can be found in [5].

To check the consistency of the comparison of the shifted data with CT10NNLO predictions, Fig. 13 shows histograms of the residuals, as defined in Eq. (26), for six bins of the jet rapidity ( $y$ ). The distributions observed in the histograms appear to be reasonably consistent with the superimposed standard normal distribution, within the limitations of the small number of data points in each  $y_j$  bin.

We also check the size of the optimal shift parameters  $\{\bar{\lambda}_\alpha; \alpha = 1, 2, 3, \dots, 23\}$  and find that the histogram of the parameters shown in Fig. 14 is also consistent with the standard normal distribution. According to the figure, no unreasonable shifts are required to create agreement between the theory and the data. Some of the systematic errors have a larger impact on the jet cross section than others, such as those related to the jet energy scale uncertainties.

A comparable measurement of inclusive jet production was performed by the CDF collab-

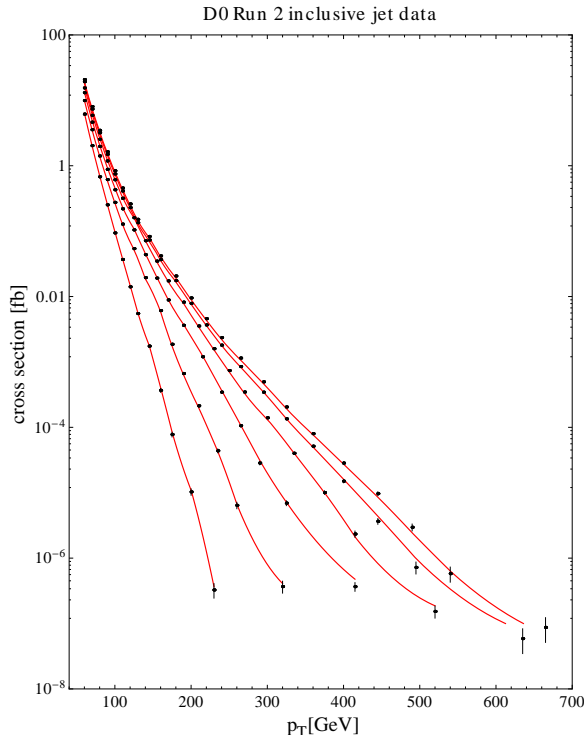


FIG. 12: Data and theory for the inclusive jet production data at DØ Tevatron Run-2. The black points represent central values of the data, error bars are uncorrelated errors, and red curves are NLO theory obtained by using CT10NNLO PDFs.

oration in Run-2 [83]. This jet measurement has different systematic uncertainties than DØ, and hence provides an independent constraint on the PDF parameters. A similar investigation indicates that the CT10 PDFs agree well with the CDF measurement. Fig. 15 compares the CDF data set for inclusive jet production and the CT10 prediction, and the corresponding histogram of the residuals is shown in Fig. 16. The CDF value of  $\chi_E^2/N_{pt} = 102/72 = 1.42$  is higher than for DØ, but the histograms of the residuals do not reveal pronounced systematic disagreements. The contribution of 25 systematic shifts to the  $\chi_E^2$  function of the CDF measurement is  $\chi_\lambda^2 = 18$ .

#### D. Correlated systematic errors in Tevatron jet production

The results of the previous subsection show the importance of experimental systematic uncertainties in describing the Tevatron jet data. These uncertainties can be generally of two kinds, additive and multiplicative. For example, the underlying event and pileup uncertainties are additive errors. They are determined independently of the jet cross section. The luminosity uncertainty and jet energy scale (JES) uncertainty are multiplicative errors. From the start, they are estimated as the percentage of the jet cross section in each bin. In jet production, there is no reason to handle the luminosity uncertainty differently from the

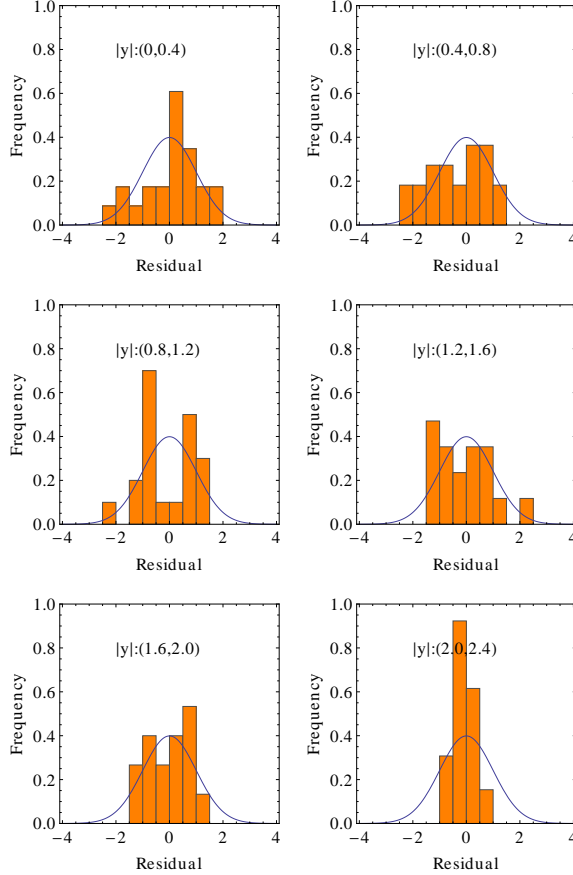


FIG. 13: Histograms of residuals for the DØ Tevatron Run-2 inclusive jet production data. Residuals are defined in Eq. (26). The solid curve is the standard normal distribution, for comparison.

JES and other multiplicative errors, as most of them have a comparable impact on the fit.<sup>7</sup> Often, it is unknown if the error is additive or multiplicative. All of them are reconstructed from the published percentage values according to one of the methods that were reviewed in Sec. III C.

Both the QCD scale dependence of NLO jet cross sections and the detailed implementation of the systematic errors were explored when preparing our NNLO set of PDFs. An assortment of NNLO gluon PDF shapes, obtained by various treatments of jet production data in the global analysis and normalized to the shape of the CT10W NLO gluon PDF, is illustrated in Fig. 17. We compare five methods for the computation of  $\beta_{i,\alpha}$  in jet production (cf. Sec. III C) and several choices of the renormalization and factorization scale. The CT10

<sup>7</sup> In the CTEQ6.X series and some other previous fits, the normalization of each experiment was fitted as a separate free parameter with a  $\chi^2$  penalty imposed on its deviation from the nominal value. The procedure used was similar to the “normalization penalty trick” discussed in Ref. [59]. In the CT10 fits, the normalization uncertainty is instead included in the correlation matrix  $\beta_{i,\alpha}$  and treated similarly to other multiplicative errors.

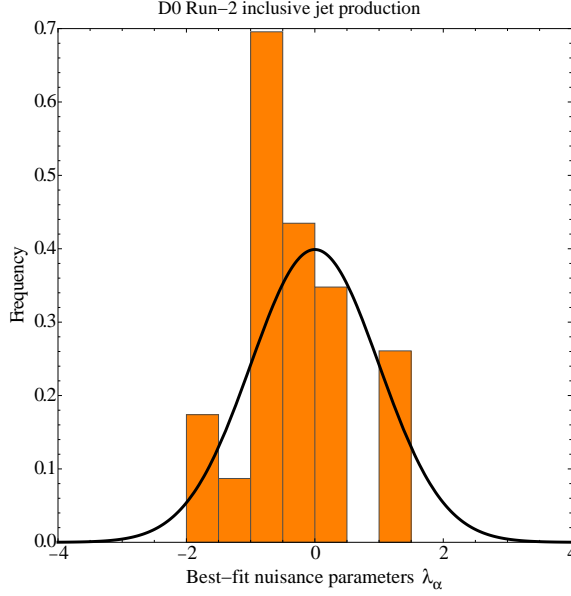


FIG. 14: Histogram of the optimal systematic shifts  $\{\bar{\lambda}_\alpha\}$  for the DØ Tevatron Run-2 inclusive jet production data.

central set and its PDF error band, both obtained by assuming method  $D$  for computing  $\beta_{i,\alpha}$  and the QCD scale  $\mu = P_{Tj}$ , are shown by the solid black line and shaded green region, respectively. For data sets other than the jet data in the global fit, we consistently use the extended  $T$  definition of  $\beta_{i,\alpha}$ .

If the Run-2 jet cross sections are not included in the calculation of the global  $\chi^2$  (or included with a small weight, such as 0.01), the fit generally prefers a softer gluon PDF at  $x > 0.1$ , as indicated by the magenta long-dashed line in the figure. If  $\alpha_s(M_Z)$  is fitted as well, its NNLO value in a fit without the jet data sets is also low, of order 0.114.

With the jet data included, there is a general preference for an enhanced  $g(x, Q)$  at large  $x$ , with some possible outcomes shown in Fig. 17. The curves were obtained using the extended  $T$ ,  $T$ , and  $D$  methods, for the factorization scales  $\mu = P_{Tj}/2, P_{Tj}, 2P_{Tj}$ , with  $P_{Tj}$  being the transverse momentum of an individual jet in each  $P_T$  bin. Both the original method  $T$  (applied only to the luminosity error) and extended method  $T$  (applied to all correlated errors) produce a robust increase in  $g(x, Q)$  at  $x > 0.2$ , but the shape and magnitude of the enhancement vary with  $\mu$ . The  $D$  method (black solid curve) results in a softer shape of the best-fit  $g(x, Q)$  which lies between the fits with and without the jet data. All these curves lie well within the PDF error band of the public CT10 NNLO set.

A complementary perspective is provided by Fig. 18, comparing the gluon PDF  $g(x, Q)$  at  $Q = 85$  GeV obtained with the five methods for computation of  $\beta_{i,\alpha}$  and the same factorization scale  $\mu = P_{Tj}$  in FASTNLO jet cross sections. All the curves are normalized to the CT10 NNLO prediction (based on the  $D$  method). Here, we observe some differences between the (extended)  $T$  and  $T^{(0)}$  prescriptions. The extended  $T$  method results in a drastic enhancement of  $g(x, Q)$  at  $x > 0.3$ , which is tempered when using the extended  $T^{(0)}$

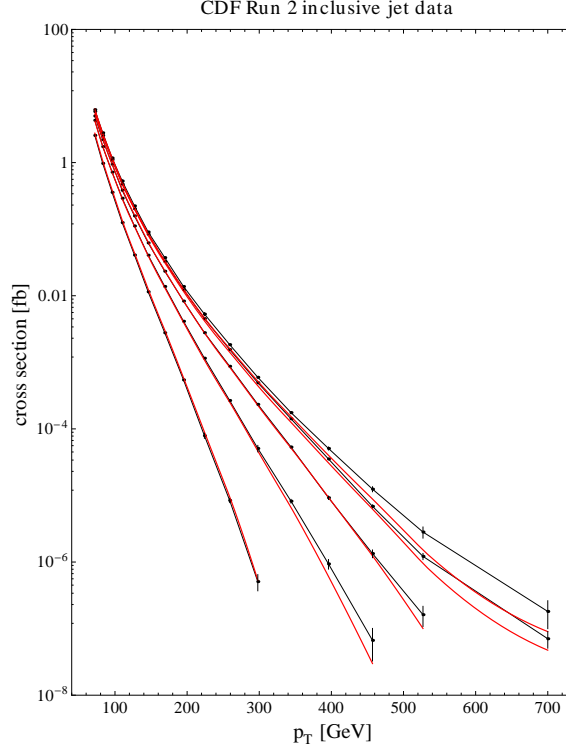


FIG. 15: Data and theory for inclusive jet production at CDF Tevatron Run-2. The black points are the central values of the data, the error bars are uncorrelated errors, and the red curves represent the NLO predictions computed by using CT10NNLO PDFs.

method. The  $T$  and  $T^{(0)}$  methods produce a stronger enhancement at  $0.05 < x < 0.3$ , but are flatter for  $x > 0.3$ .

Parameter	Type of the fit	Method for computing $\beta_{i,\alpha}$				
		$D$	$T$	$T^{(0)}$	Ext. $T$	Ext. $T^{(0)}$
$\bar{\chi}_E^2/N_{pt}$ for CDF ( $N_{pt} = 72$ ) and DØ ( $N_{pt} = 110$ )	PDF only	1.42, 1.04	1.23, 1.05	1.21, 1.04	1.48, 1.03	1.49, 1.03
	PDF+ $\alpha_s$	1.33, 0.95	1.24, 1.07	1.23, 1.06	1.48, 1.06	1.51, 1.08
$\bar{\lambda}_{\text{lumi}}$	PDF only	1.2, 1.3	-1.4, -1.2	-1.5, -1.3	0.53, 0.90	0.61, 0.96
	PDF+ $\alpha_s$	2.7, 2.8	-0.71, -0.51	-0.75, -0.55	1.2, 1.5	1.4, 1.8
$\bar{\alpha}_s(M_Z)$	PDF only	0.118	0.118	0.118	0.118	0.118
	PDF+ $\alpha_s$	0.1137	0.1159	0.1159	0.1162	0.1159

TABLE II: Best-fit values of  $\chi_E^2/N_{pt}$  and the luminosity nuisance parameter  $\lambda_{\text{lumi}}$  for the Tevatron Run-2 inclusive jet production, and for  $\alpha_s(m_Z)$  in a fit with floating  $\alpha_s(M_Z)$ . The columns are obtained with the five methods for including correlated systematic errors in jet production. The first (second) numbers in each column correspond to the CDF (DØ) data sets, respectively.

In all of the listed fits to the jet data, the quality of the fits are generally comparable. Table II shows representative output quantities for five methods:  $\chi^2/N_{pt}$  for the CDF Run-2 and DØ Run-2 jet data sets, the best-fit luminosity parameter  $\lambda_{\text{lumi}}$ , and the best-fit  $\alpha_s(M_Z)$  (if fitted). In all fits, the values of  $\chi^2/N_{pt}$  are similar, with the  $T/T^{(0)}$  methods showing



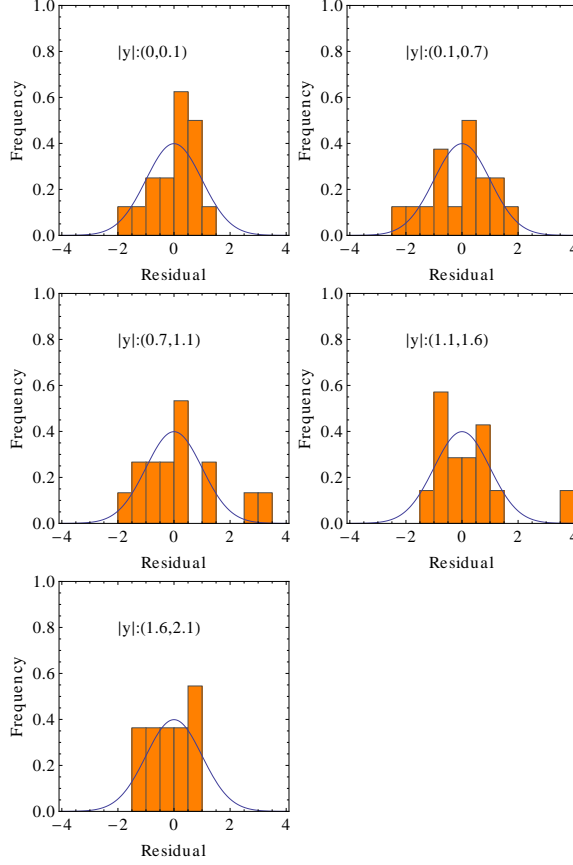


FIG. 16: Histogram of residuals (defined in Eq. (26)) for the CDF Run-2 inclusive jet production.

a marginally better agreement with the CDF jet data ( $\chi^2/N_{pt} \approx 1.23$  vs. 1.4-1.5). If the QCD coupling strength is fixed in the fit to be  $\alpha_s(M_Z) = 0.118$ , all luminosity shifts do not exceed 1.5 standard deviations, see the lines referring to “PDF only” fits.

However, if  $\alpha_s(M_Z)$  is also fitted (the “PDF+ $\alpha_s$ ” fits), in the  $D$  method we obtain a *low*  $\alpha_s(M_Z)$  of 0.1137, accompanied by a *large* luminosity shift  $\bar{\lambda}_{\text{lumi}} \approx 2.7$ . The  $D$  method also results in a low  $\chi^2/N_{pt}$  combination of 1.33 and 0.95.

With four other methods, we obtain higher best-fit values of  $\alpha_s(M_Z) \approx 0.116$ , higher  $\chi^2$  values, and the luminosity shifts below  $2\sigma$ . This peculiarity of the “PDF+ $\alpha_s$ ” fit employing the  $D$  method is suggestive of a strong D’Agostini bias. It does not occur at the same level in the “PDF only” fits that use a fixed  $\alpha_s(M_Z)$ , including CT10 NNLO.

As can be seen from Fig. 17, by using method  $D$  to determine the published CT10 NNLO set and the QCD scale  $\mu = P_{Tj}$ , we obtain a PDF uncertainty band that also covers the gluon PDF parametrizations found with the alternative methods for the correlation matrix and choices of QCD scales. The softer gluon behavior than in CT10W NLO is consistent with the preference of the non-jet experiments and results in lower  $\chi^2$  for the combined HERA DIS set. It may also simulate the anticipated effect of missing NNLO corrections

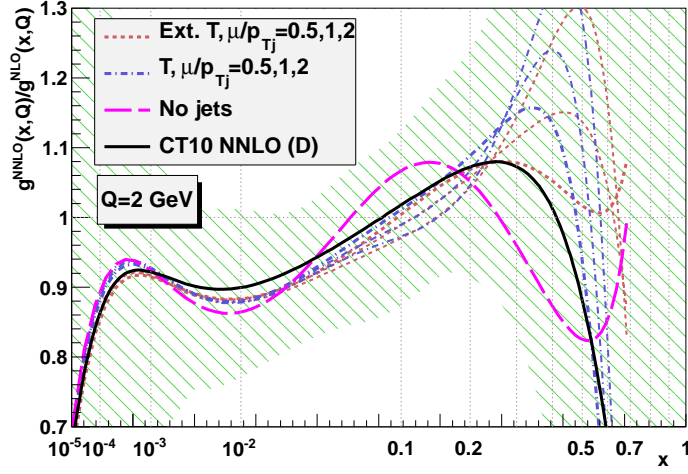


FIG. 17: Comparison of NNLO gluon PDF parametrizations obtained using different procedures for including jet production data sets in the global fit.

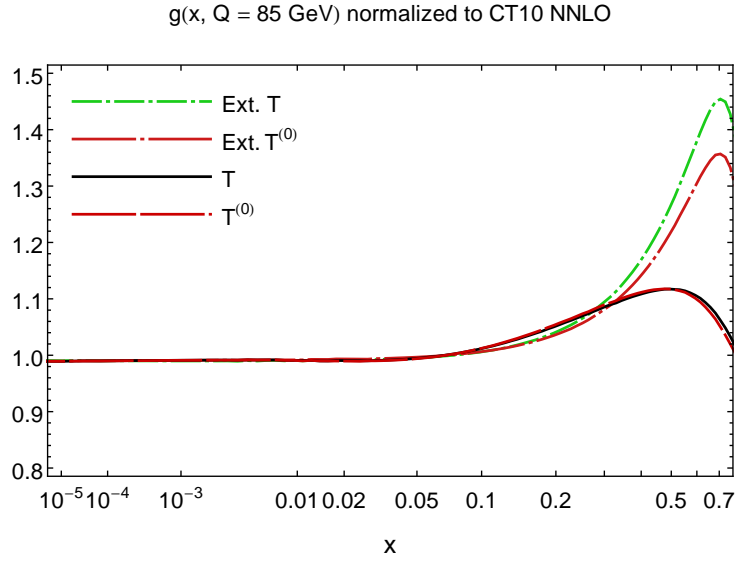


FIG. 18: Dependence of the gluon PDF on various definitions of the correlation matrices  $\beta_{i\alpha}$  for the Tevatron Run 2 jet data in the global fit.

on the jet cross sections. The uncertainty band for  $g(x, Q)$  in Fig. 17 thus represents the current level of uncertainty in predicting the inclusive jet cross sections, due to variations in the fit procedure. These variations are typically smaller than the PDF error determined by the Hessian method.

## VII. COLLIDER PHENOMENOLOGICAL PREDICTIONS

A number of standard model cross section measurements from the LHC have been published, at center-of-mass energies of 7 and 8 TeV. Differential distributions are available from the 7 TeV data (taken in 2010 and 2011), while the current 8 TeV results (2012) are mostly in the form of inclusive cross section measurements. In this section, we use the CT10 PDFs presented in this paper to determine theory predictions for several important LHC cross sections, including the production of electroweak gauge bosons, inclusive jets, and top pairs. We compare the resulting predictions with the most recent corresponding LHC data sets. These data sets have not been used in the determination of the CT10 PDFs, but will be used in future fits.

We also compare some of the CT10 predictions to those based on other NNLO PDFs: NNPDF2.3 [25], HERAPDF1.5 [28, 29], and MSTW2008 [24]. All calculations use the native value of  $\alpha_s(m_Z)$  for the PDF set; the PDF uncertainties are shown at the 68% c.l. For the results from HERA PDFs we only include the uncertainties from the standard eigenvector sets. We do not consider the  $\alpha_s$  uncertainties.

The LHC standard model cross sections are calculated with the following settings.

- For electroweak gauge boson production, the total cross sections are computed at NNLO using the program FEWZ2.1 [93, 94] and the factorization scale  $Q = M_V$ . The differential cross sections and asymmetries with cuts on transverse momenta of the leptons are computed with the code RESBOS [95, 96] that realizes the NNLL resummation of logarithms at small transverse momentum. The settings of the RESBOS computation and nonperturbative function are the same as in [97], including the hard QCD scale that is equal to  $M_V/2$ . This calculation provides a close approximation to the NNLO resummed cross section. The needed two-loop coefficients are obtained from the  $\mathcal{O}(\alpha_s^2)$  cross sections at large transverse momentum [98, 99] and by requiring that the RESBOS total rate coincides with the inclusive NNLO rate [100] computed by the CANDIA code [101, 102].
- The cross section for top quark pair production is computed by the TOP++ code (version 1.4) [103]. The factorization and renormalization scale is chosen as  $Q = m_t$ , the top quark mass is  $m_t = 172.5$  GeV [104], and the other settings are as in Ref. [105]. The calculation includes the exact NNLO corrections to the  $q\bar{q} \rightarrow t\bar{t}$  production [106] and an approximate NNLO combined with NNLL threshold logarithms in the other channels. Hence, the calculation provides a close to exact NNLO prediction at the Tevatron, where the  $q\bar{q}$  channel dominates, and an approximate NNLO prediction at the LHC, where top production takes place primarily from  $gg$  initial states.
- Higgs boson production cross sections in the gluon-gluon fusion channel are computed at NNLO using the HNNLO code [107, 108]. The factorization and renormalization scale was taken to be  $Q = m_H = 125$  GeV, consistent with the recommendation of the LHC Higgs cross section working group [109]. Higgs production in the bottom quark fusion channel is computed at NNLO using the BBH@NNLO v1.3 code [110].

- LHC inclusive jet cross sections are computed at NLO with the FASTNLO code [88–90] and cross checked against the MEKS code in [58, 86]. The central scale in these predictions is chosen to be  $\mu = P_{Tj}$ , the transverse momentum of each jet.

### A. W and Z total cross sections

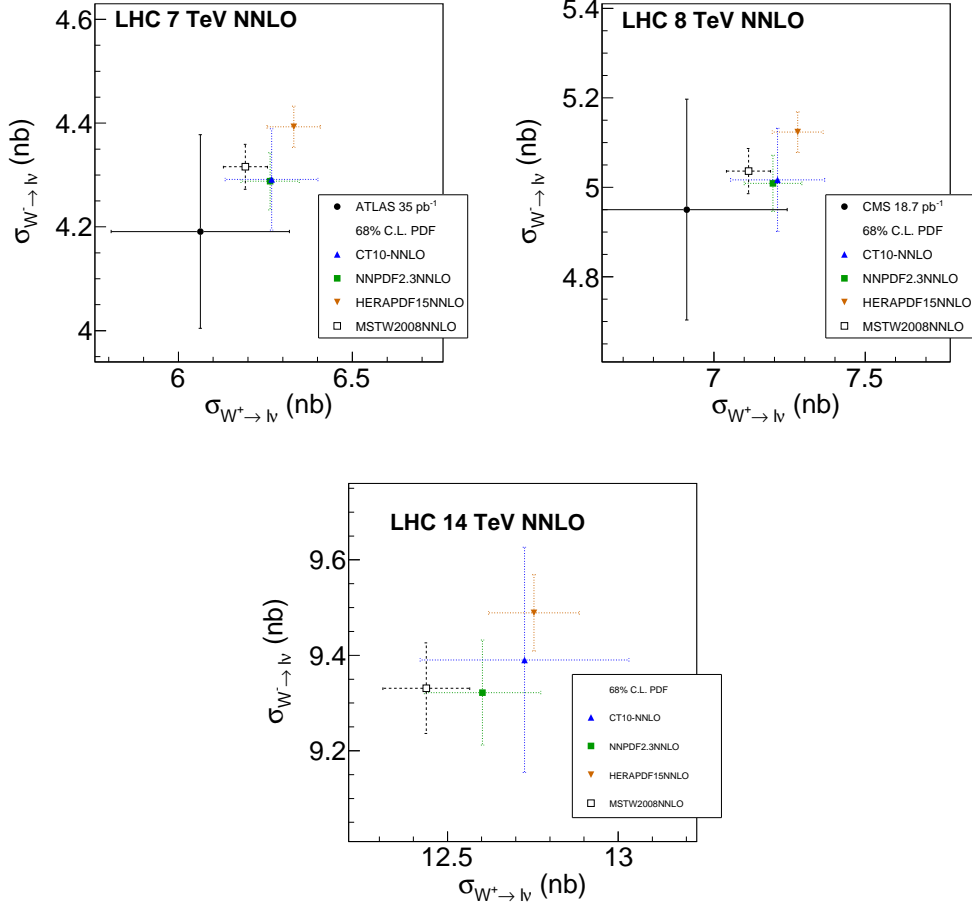


FIG. 19: NNLO  $W^+$  and  $W^-$  cross sections at the LHC.

In Fig. 19, we show predictions at NNLO for  $W^\pm$  production at 7, 8 and 14 TeV, compared to ATLAS data at 7 TeV [111] and CMS data at 8 TeV [112]. The CT10 NNLO predictions are in good agreement both with the data and predictions from the other NNLO PDFs listed. The central values of the data are below all NNLO predictions, but are within the uncertainties. Among all PDF sets, HERAPDF predicts the largest cross sections. For simplicity, the error bars for the theoretical predictions indicate the symmetric PDF uncertainties at 68% c.l. Generally, the PDF errors of the  $W^+$  and  $W^-$  are strongly correlated [4], but the 68% c.l. error ellipses overlap well for all PDF sets.

In Figure 20, we show the NNLO predictions for the  $W^\pm$  and  $Z$  total cross sections at

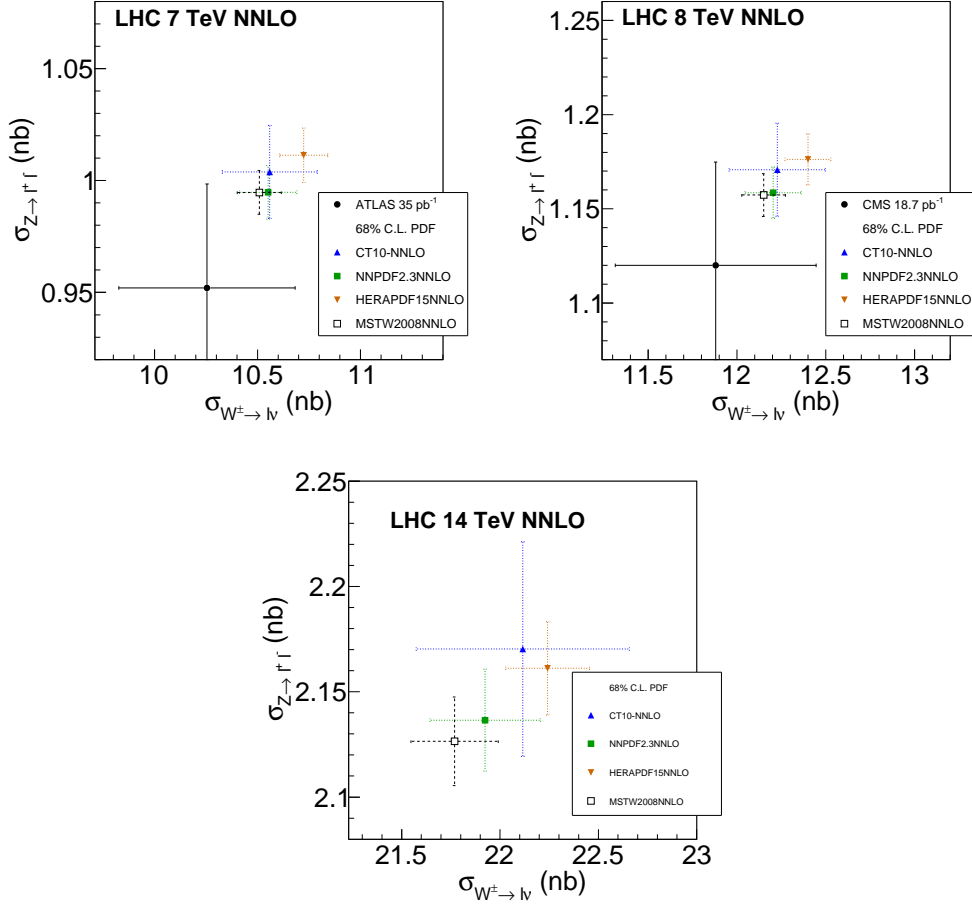


FIG. 20: NNLO  $W^\pm$  and  $Z$  cross sections at the LHC.

7, 8 and 14 TeV, again compared to ATLAS data at 7 TeV [111] and CMS data at 8 TeV [112]. The conclusions are broadly similar to those for the  $W^+$  and  $W^-$  comparisons.

## B. Top quark pair production, total cross sections

In Fig. 21, we show the combined Tevatron total cross section for  $t\bar{t}$  production [113] and ATLAS [114–118] and CMS [119] total cross sections, compared to approximate NNLO predictions. The experimental central values and uncertainty ranges are indicated by vertical lines and colored rectangles. For each collider energy, all cross sections are normalized to the respective CT10NNLO prediction. Again, we observe good agreement between CT10NNLO and other theoretical predictions as well as the data.

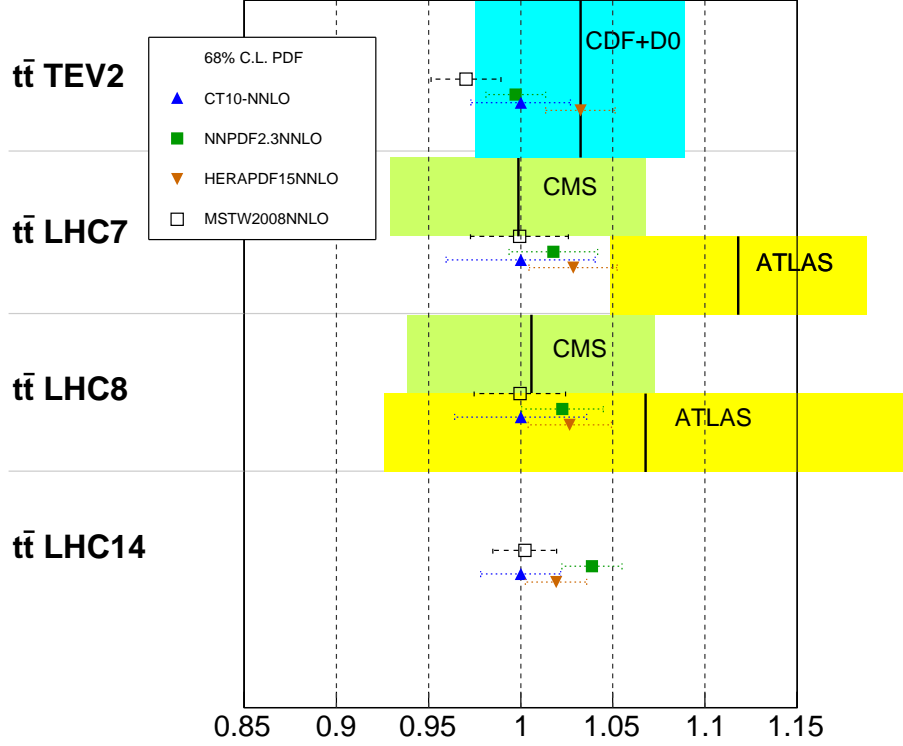


FIG. 21: Approximate NNLO predictions and experimental measurements of  $t\bar{t}$  total cross sections at the Tevatron and LHC, normalized to CT10NNLO predictions.

### C. W and Z rapidity distributions

More detailed PDF information can be gained by comparisons to  $W/Z$  rapidity distributions and  $W$  charge lepton asymmetry from ATLAS [111], CMS [120], and LHC-B [121] at 7 TeV. For differential observables, we use RESBOS to account for multiple soft gluon radiation that may be non-negligible in the presence of constraints on the charged lepton's transverse momentum  $p_{T\ell}$ . Typical  $W/Z$  production measurements require  $p_{T\ell}$  to be above 20-25 GeV in order to suppress charged leptons from background processes, and because of trigger requirements.

In some measurements, the lower  $p_{T\ell}$  cut is as high as 35 GeV, approaching the position of the Jacobian peak in  $d\sigma/dp_{T\ell}$  at  $p_{T\ell} \approx M_W/2 \approx 40$  GeV (for  $W$  boson production), where large logarithms  $\ln(Q_T/Q)$  dominate. ( $Q$  and  $Q_T$  denote the invariant mass and transverse momentum of the weak boson, respectively.) With such high  $p_{T\ell}$  cuts, the RESBOS resummation calculation, which resums large logarithmic contributions to all orders in strong coupling, is expected to provide a better description of the data than the fixed-order calculations [93, 122, 123]. In practical comparisons, differences between the resummed and fixed-order NNLO calculations are most pronounced with an *upper* cut close to  $p_{T\ell} \approx Q/2$

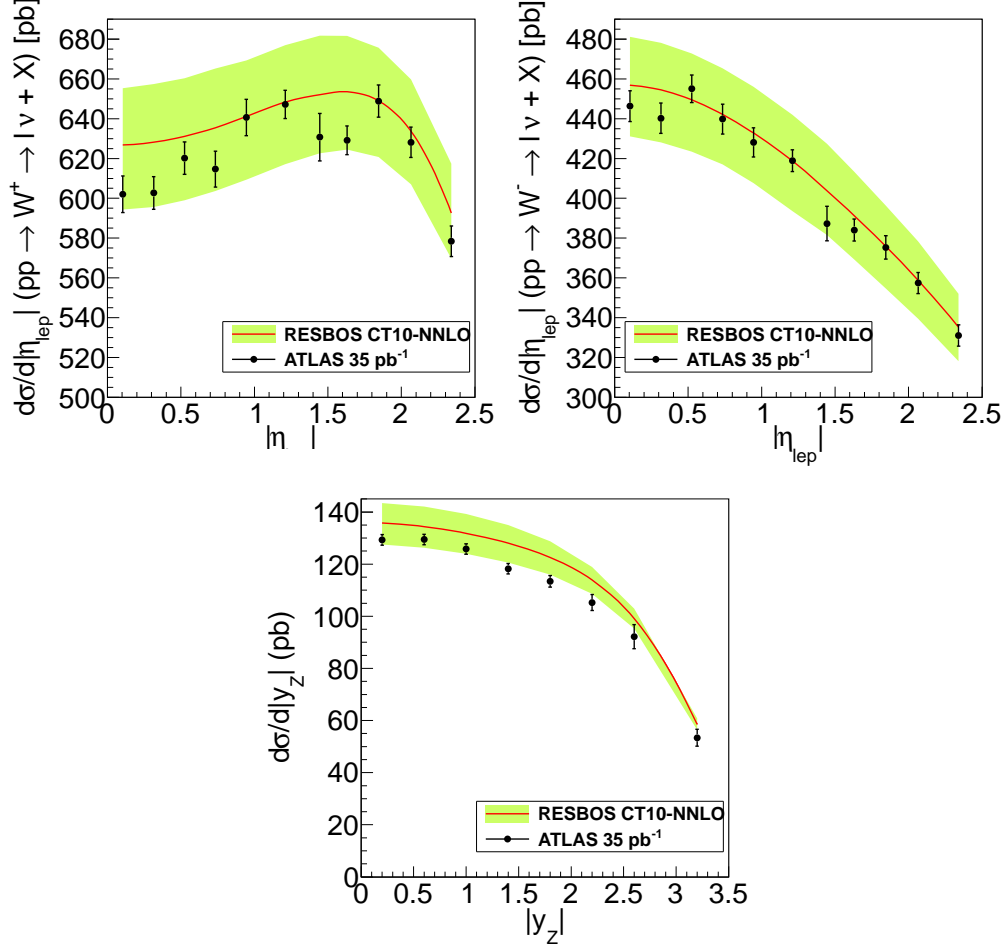


FIG. 22: Rapidity distributions of  $Z$  and  $W^\pm$  cross sections in ATLAS ( $35 \text{ pb}^{-1}$ ) measurements at 7 TeV.

[124]. The resummed and NNLO asymmetries are closer in general when only a *lower* cut is imposed.

In Fig. 22 we show a comparison between predictions for the  $Z$  and  $W^\pm$  lepton rapidity distributions and the data measured by the ATLAS collaboration using  $35 \text{ pb}^{-1}$  of integrated luminosity at 7 TeV [111]. In all three figures the green band represents the PDF uncertainty, while the red solid line shows the central prediction. For the  $Z$  rapidity distribution, the central RESBOS prediction overshoots the data by a few percent, but is within the PDF uncertainties from the data. These LHC  $Z/W^\pm$  data are yet to be included in the fits and may modify the quark PDFs at small  $x$ . It is interesting to note that ATLAS found that the tight constraints on the relevant normalization between the  $W$  and  $Z$  data sets resulted in a larger-than-expected strange quark density in the  $x$  range represented by the  $Z$  and  $W^\pm$  lepton rapidity distributions [125]. We shall include these (and upcoming) data sets, with correlated systematic error analysis, in our next run of global analysis.

In Fig. 23, a RESBOS prediction is compared to the lepton charge asymmetry from ATLAS and LHC-B [121] at 7 TeV as a function of the lepton pseudorapidity  $\eta_{\text{lep}}$ . The



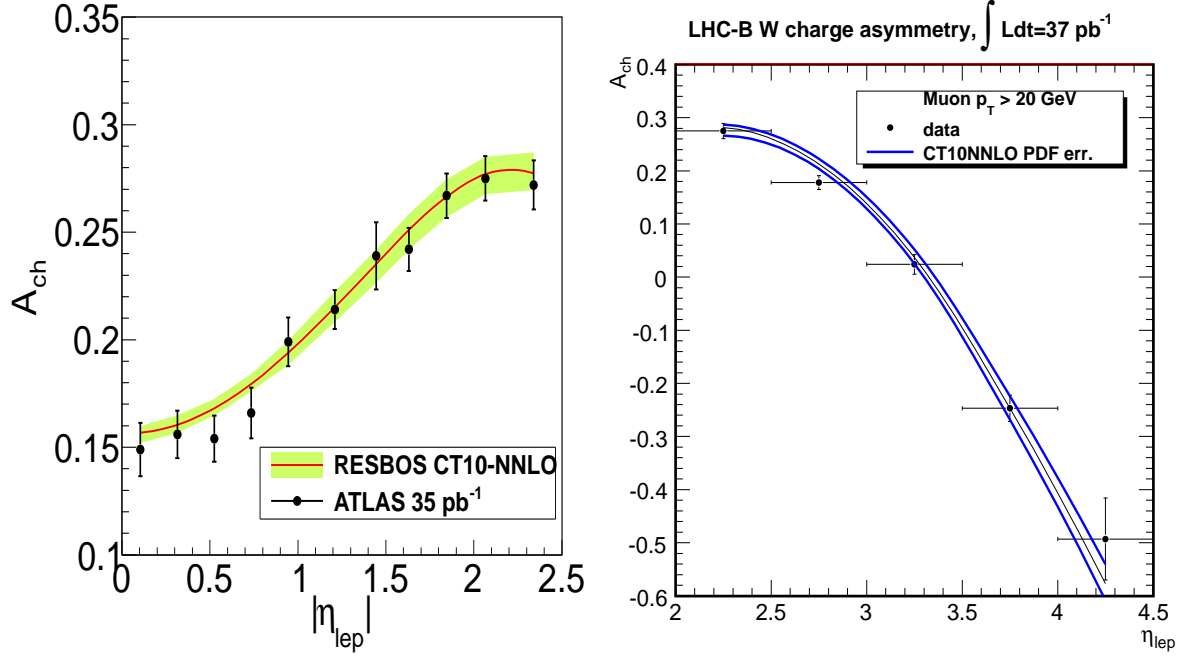


FIG. 23: A lepton rapidity distribution of the  $W^\pm$  charge asymmetry in the ATLAS (35  $\text{pb}^{-1}$ ) measurement (left) and LHC-B (37  $\text{pb}^{-1}$ ) measurement (right) at 7 TeV.

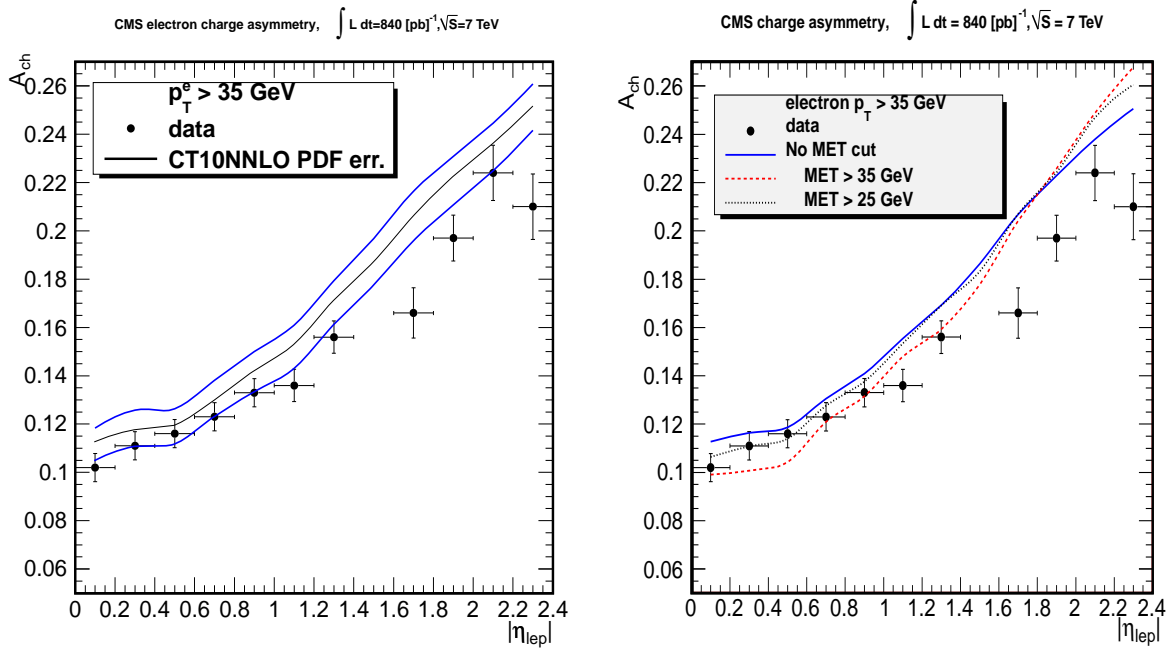


FIG. 24: A lepton rapidity distribution of the  $W^\pm$  charge asymmetry in the CMS (840  $\text{pb}^{-1}$ ) measurement at 7 TeV.

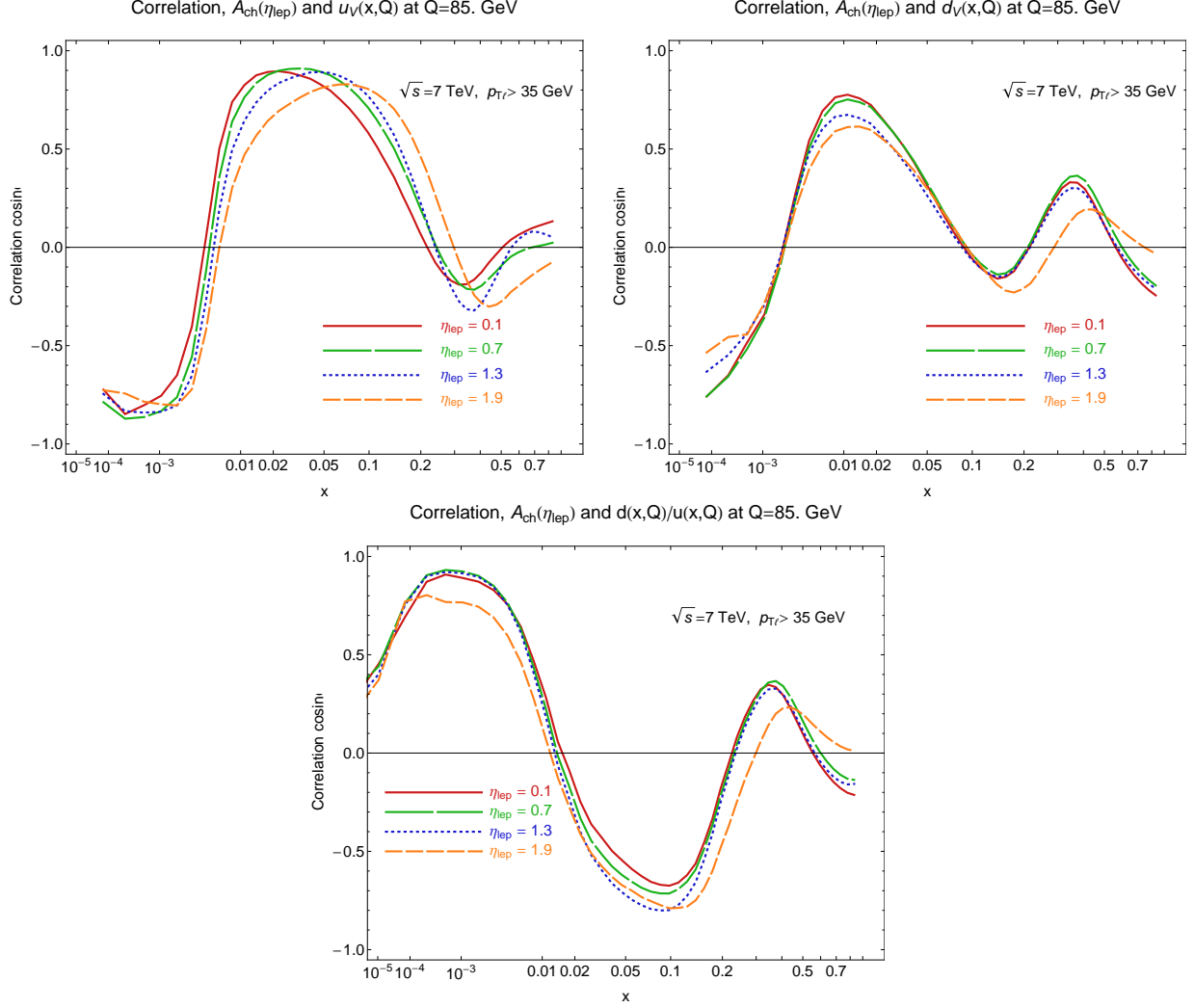


FIG. 25: PDF-induced correlations between  $W$  charge asymmetry  $A_{ch}(\eta_{lep})$  at the LHC 7 TeV and  $u_v(x, Q) = u(x, Q) - \bar{u}(x, Q)$ ,  $d_v(x, Q) = d(x, Q) - \bar{d}(x, Q)$ , and  $d(x, Q)/u(x, Q)$  at  $Q = 85$  GeV. The charge asymmetry is evaluated at lepton rapidity values indicated in the figure.

agreement of CT10 NNLO with both asymmetry sets is good, *e.g.*  $\chi_E^2/N_{pt} = 0.45$  for ATLAS  $W$  asymmetry. The LHC-B experiment probes a different kinematic range (more forward coverage) than either ATLAS or CMS, and thus can provide unique information on large- $x$  quark distributions. In this figure, the central prediction and PDF error are indicated by the black solid and blue solid lines, respectively.

The LHC  $W$  charge asymmetry measurements have the potential to test some combinations of the PDFs that are still poorly constrained. For example, the measurement of the charge asymmetry in the rapidity bins of CMS in Fig. 24 probes *valence* quark PDFs,  $u_v(x, Q) \equiv u(x, Q) - \bar{u}(x, Q)$  and  $d_v(x, Q) \equiv d(x, Q) - \bar{d}(x, Q)$  in the small- $x$  region that is not constrained by the previous data.

Fig. 25 shows the PDF-induced correlation cosine  $\cos \varphi$  [4, 53] between the LHC  $W$

charge asymmetry in several bins of lepton rapidity  $\eta_{lep}$  and valence  $u$  and  $d$  quark PDFs and the ratio  $d(x, Q)/u(x, Q)$  of the CT10NNLO PDF set. In the intervals of  $x$  where  $\cos \varphi$  is close to  $\pm 1$ , the  $W$  asymmetry data at the shown  $\eta_{lep}$  values is sensitive to the PDF uncertainty on the indicated parton distributions. A strong correlation can be observed with  $u_v$  at  $0.01 < x < 0.15$  and  $d_v$  at  $0.005 < x < 0.05$ . Both valence PDFs show a strong anticorrelation at  $x < 0.001$  as a consequence of the valence sum rules. The  $d/u$  ratio shows a strong correlation at  $0.0005 < x < 0.005$  and anticorrelation at  $0.05 < x < 0.2$ . The other PDF flavors are not strongly correlated with the  $W$  asymmetry in these rapidity ranges.

The current CMS  $W$  asymmetry data shown in the left panel of Fig. 24 agrees reasonably with the CT10 NNLO PDFs, given the present PDF uncertainties and experimental uncertainties. The CMS data is slightly below the central CT10 prediction at  $|\eta_{lep}| < 1$ , but within the PDF uncertainty band. The disagreement is increased at  $|\eta_{lep}| < 2$ , where we also observe less regular behavior of the data.

We note that the reconstruction of the present CMS data has a systematic uncertainty associated with the discrimination from background processes. In the Tevatron  $W$  asymmetry measurements, it was essential to require a sufficiently high missing  $E_T$  (MET), of order 20 GeV or more, to discriminate the  $W$  boson decay events from the significant background. The MET requirement has not been imposed in the current CMS measurement, which applied a different technique to suppress the background.

In the ResBos theoretical calculation, we cannot exactly implement the experimental background subtraction technique when comparing to the CMS data. At the lowest order in PQCD (when  $Q_T = 0$ ), the additional MET cut is not needed, as the condition  $p_{Tl} > 35$  GeV automatically implies  $MET > 35$  GeV. At higher orders, the  $p_{Tl}$  and MET cuts are no longer equivalent. The predictions for  $W$  charge asymmetry depend on the assumed MET cut, cf. the right panel in Fig. 24. This behavior suggests that subtle effects in the separation of  $W$  boson events from the background may be comparable to the observed differences between CT10 NNLO theory and CMS data in Fig. .

In the absence of applicable experimental constraints in the CT10 fit, the small- $x$  behavior of the  $u_v$  and  $d_v$  PDFs is assumed to be governed by a shared  $x$  power,  $u_v(x, Q_0), d_v(x, Q_0) \sim x^{A_{1v}}$  in the  $x \rightarrow 0$  with the same  $A_{1v} \approx -1/2$ . This Regge-inspired assumption partly explains the correlations of PDFs at small  $x$ . It will be tested by including the LHC  $W$  asymmetry in the upcoming fits.

#### D. ATLAS inclusive jet distribution

In Figs. 26 and 27, we compare the inclusive cross section predictions to the ATLAS measurements using the anti- $k_T$  jet algorithm with  $R = 0.6$ . In Fig. 26, the comparisons are made to the ATLAS raw, unshifted data; in Figs. 27, the optimal systematic shifts have been applied to the ATLAS central values. The scale uncertainty in the theory prediction is calculated by varying the QCD scale in the range  $P_{Tj}/2 \leq \mu \leq 2P_{Tj}$ . The uncertainties of the data points shown in Figures 26 and 27 are evaluated by adding the statistical and uncorrelated systematic errors in quadrature.

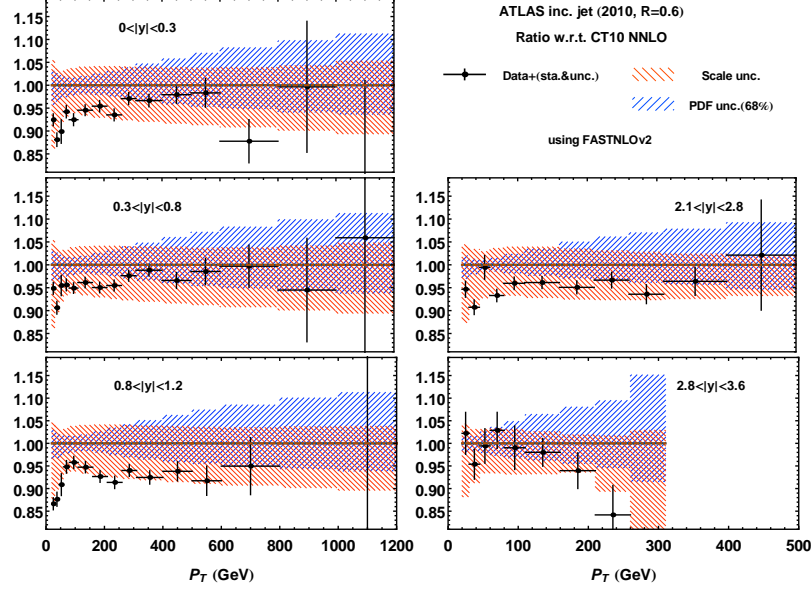


FIG. 26: Comparison of CT10NNLO predictions with unshifted 2010 ATLAS inclusive jet data ( $R = 0.6$ ).

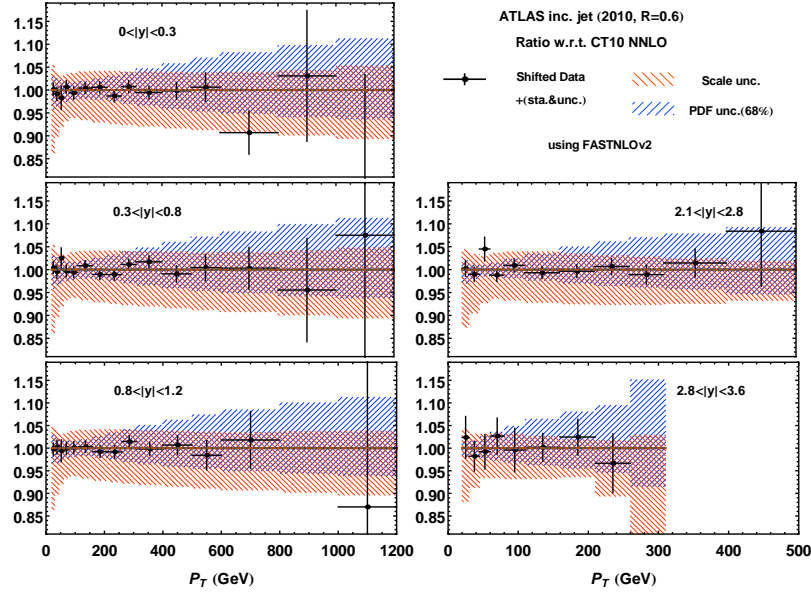


FIG. 27: Comparison of CT10NNLO predictions with shifted 2010 ATLAS inclusive jet data ( $R = 0.6$ ).

The overall agreement of the shifted data with the (NLO) predictions utilizing CT10NNLO PDFs is good even without theory uncertainty:  $\chi^2_E/N_{pt} = 0.74$  (0.78) for  $R = 0.6$  (0.4). Some differences in the shape and normalization observed for the unshifted data disappear upon application of the systematic error shifts. The  $\chi^2_E$  function is defined according to the extended  $T$  convention for the ATLAS correlation matrix. Slightly higher

values of  $\chi_E^2$  would be obtained with alternative conventions for  $\beta_{i,\alpha}$  [58]. An in-depth comparison of theoretical jet cross sections based on CT10NNLO to the 2010 ATLAS data and predictions based on other PDF sets is documented in [58]. In that paper, we examine the uncertainties in the current NLO predictions compared to the experimental accuracy and discuss prospects for constraining the PDFs with the upcoming LHC jet data.

### E. SM Higgs boson total cross sections

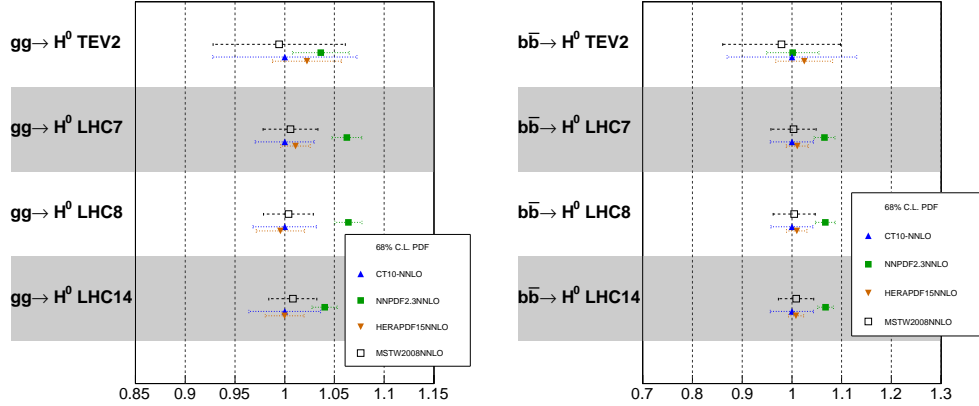


FIG. 28: NNLO cross sections of SM Higgs boson production via gluon fusion (left) and bottom quark annihilation (right), normalized to CT10NNLO predictions.

Now we turn to the NNLO total cross sections for Higgs boson production at both the Tevatron and LHC via gluon-gluon fusion [107, 108] and  $b\bar{b}$  annihilation [110], shown as ratios to the CT10NNLO prediction in Fig. 28. At the Tevatron, PDF uncertainties of the Higgs boson production cross section via gluon-gluon fusion are large and cover all the central predictions. At the LHC, the CT10NNLO gluon-gluon fusion predictions are in a good agreement with those from the other PDF groups, except for NNPDF2.3 at 7 and 8 TeV, which predicts larger cross sections. For Higgs boson production via  $b\bar{b}$  annihilation, the NNLO predictions obtained with all PDFs are consistent within the quoted PDF uncertainties.

## VIII. DISCUSSION AND CONCLUSION

We have presented next-to-next-to-leading order (NNLO) parton distribution functions (PDFs) from the CTEQ-TEA group. These CT10NNLO PDFs have been determined based on essentially the same global data sets used in the previous CT10 and CT10W NLO PDF analyses. In this new analysis, the effects of finite quark masses have been implemented in

the S-ACOT- $\chi$  scheme at NNLO accuracy. We obtain a similar quality of agreement with the fitted experimental data sets in the NNLO fit as at NLO.

We find that at low  $x$  (below  $10^{-2}$ ), the NNLO gluon distribution is suppressed, while the quark distributions increase, compared to the same distributions at NLO. The  $\mathcal{O}(\alpha_s^2)$  GM VFN scheme used in the NNLO fit results in changes to the heavy quark distributions, both charm and bottom. The large- $x$  gluon and  $d$ -quark distributions are reduced due to (1) the removal of the Tevatron Run-1 inclusive jet data, (2) the alternate treatment of correlated systematic errors and choices of renormalization and factorization scales in jet cross sections, and (3) revised electroweak couplings in DIS cross sections.

Compared to the MSTW2008 NNLO PDFs, the gluon and quark distributions are larger as  $x$  approaches zero (the CT10 parameterization requires a positive gluon), while the strangeness distribution is larger over most of the  $x$  range. The differences tend to decrease as  $Q^2$  increases.

We have compared NNLO predictions using CT10 to available LHC data and have found good agreement. Numerical comparisons presented here complement a more detailed benchmark study of the LHC predictions that has been recently released [58]. The available LHC data is already providing important information on PDFs, and future data will provide even stronger constraints. This will be developed further in a future publication.

## Acknowledgments

This work was supported by the U.S. DOE Early Career Research Award DE-SC0003870 and by Lightner-Sams Foundation; by the U.S. Department of Energy under Grant No. DE-FG02-96ER40969; by the U.S. National Science Foundation under Grant No. PHY-0855561; by the National Science Council of Taiwan under Grant Nos. NSC-98-2112-M-133-002-MY3 and NSC-101-2112-M-133-001-MY3.

- 
- [1] J. Pumplin, D. Stump, J. Huston, H.-L. Lai, P. M. Nadolsky, et al., JHEP **0207**, 012 (2002), hep-ph/0201195.
  - [2] D. Stump, J. Huston, J. Pumplin, W.-K. Tung, H.-L. Lai, et al., JHEP **0310**, 046 (2003), hep-ph/0303013.
  - [3] W.-K. Tung, H.-L. Lai, A. Belyaev, J. Pumplin, D. Stump, et al., JHEP **0702**, 053 (2007), hep-ph/0611254.
  - [4] P. M. Nadolsky, H.-L. Lai, Q.-H. Cao, J. Huston, J. Pumplin, et al., Phys.Rev. **D78**, 013004 (2008), 0802.0007.
  - [5] J. Pumplin, J. Huston, H.-L. Lai, P. Nadolsky, W.-K. Tung, et al., Phys.Rev. **D80**, 014019 (2009), 0904.2424.
  - [6] M. Aivazis, J. C. Collins, F. I. Olness, and W.-K. Tung, Phys.Rev. **D50**, 3102 (1994), hep-ph/9312319.

- [7] J. C. Collins, Phys.Rev. **D58**, 094002 (1998), hep-ph/9806259.
- [8] M. Kramer, F. I. Olness, and D. E. Soper, Phys.Rev. **D62**, 096007 (2000), hep-ph/0003035.
- [9] W.-K. Tung, S. Kretzer, and C. Schmidt, J.Phys. **G28**, 983 (2002), hep-ph/0110247.
- [10] H.-L. Lai, M. Guzzi, J. Huston, Z. Li, P. M. Nadolsky, et al., Phys.Rev. **D82**, 074024 (2010), 1007.2241.
- [11] S. Moch, J. Vermaseren, and A. Vogt, Nucl.Phys. **B688**, 101 (2004), hep-ph/0403192.
- [12] A. Vogt, S. Moch, and J. Vermaseren, Nucl.Phys. **B691**, 129 (2004), hep-ph/0404111.
- [13] J. Sanchez Guillen, J. Miramontes, M. Miramontes, G. Parente, and O. Sampayo, Nucl.Phys. **B353**, 337 (1991).
- [14] W. van Neerven and E. Zijlstra, Phys.Lett. **B272**, 127 (1991).
- [15] E. Zijlstra and W. van Neerven, Phys.Lett. **B273**, 476 (1991).
- [16] E. Zijlstra and W. van Neerven, Nucl.Phys. **B383**, 525 (1992).
- [17] E. Laenen, S. Riemersma, J. Smith, and W. van Neerven, Nucl.Phys. **B392**, 162 (1993).
- [18] S. Riemersma, J. Smith, and W. van Neerven, Phys.Lett. **B347**, 143 (1995), hep-ph/9411431.
- [19] M. Buza, Y. Matiounine, J. Smith, R. Migneron, and W. van Neerven, Nucl.Phys. **B472**, 611 (1996), hep-ph/9601302.
- [20] C. Anastasiou, L. J. Dixon, K. Melnikov, and F. Petriello, Phys.Rev.Lett. **91**, 182002 (2003), hep-ph/0306192.
- [21] C. Anastasiou, L. J. Dixon, K. Melnikov, and F. Petriello, Phys.Rev. **D69**, 094008 (2004), hep-ph/0312266.
- [22] A. G.-D. Ridder, T. Gehrmann, E. Glover, and J. Pires (2012), 1211.2710.
- [23] A. G.-D. Ridder, T. Gehrmann, E. Glover, and J. Pires (2013), 1301.7310.
- [24] A. Martin, W. Stirling, R. Thorne, and G. Watt, Eur.Phys.J. **C63**, 189 (2009), 0901.0002.
- [25] R. D. Ball, V. Bertone, S. Carrazza, C. S. Deans, L. Del Debbio, et al., Nucl.Phys. **B867**, 244 (2013), 1207.1303.
- [26] S. Alekhin, J. Blumlein, and S. Moch, Phys.Rev. **D86**, 054009 (2012), 1202.2281.
- [27] P. Jimenez-Delgado and E. Reya, Phys.Rev. **D79**, 074023 (2009), 0810.4274.
- [28] The H1 and ZEUS Collaborations, *HERAPDF1.5 NNLO (Preliminary)*, H1prelim-11-042, ZEUS-prel-11-002.
- [29] [https://www.desy.de/h1zeus/combined\\_results/index.php?do=proton\\_structure](https://www.desy.de/h1zeus/combined_results/index.php?do=proton_structure).
- [30] P. Nadolsky, J. Gao, M. Guzzi, J. Huston, H.-L. Lai, et al. (2012), 1206.3321.
- [31] M. Guzzi, P. M. Nadolsky, H.-L. Lai, and C.-P. Yuan, Phys.Rev. **D86**, 053005 (2012), 1108.5112.
- [32] <http://www.phys.psu.edu/~cteq/>.
- [33] <https://lhapdf.hepforge.org/>.
- [34] H.-L. Lai, J. Huston, Z. Li, P. Nadolsky, J. Pumplin, et al., Phys.Rev. **D82**, 054021 (2010), 1004.4624.
- [35] S. Kretzer, H.-L. Lai, F. Olness, and W.-K. Tung, Phys.Rev. **D69**, 114005 (2004), hep-ph/0307022.
- [36] R. Thorne and R. Roberts, Phys.Rev. **D57**, 6871 (1998), hep-ph/9709442.
- [37] R. Thorne and R. Roberts, Phys.Lett. **B421**, 303 (1998), hep-ph/9711223.
- [38] M. Cacciari, M. Greco, and P. Nason, JHEP **9805**, 007 (1998), hep-ph/9803400.
- [39] S. Forte, E. Laenen, P. Nason, and J. Rojo, Nucl.Phys. **B834**, 116 (2010), 1001.2312.
- [40] M. Buza, Y. Matiounine, J. Smith, and W. van Neerven, Eur.Phys.J. **C1**, 301 (1998), hep-ph/9612398.
- [41] A. Chuvakin, J. Smith, and W. van Neerven, Phys.Rev. **D61**, 096004 (2000), hep-



- ph/9910250.
- [42] P. M. Nadolsky and W.-K. Tung, Phys.Rev. **D79**, 113014 (2009), 0903.2667.
  - [43] T. Stavreva, F. Olness, I. Schienbein, T. Jezo, A. Kusina, et al., Phys.Rev. **D85**, 114014 (2012), 1203.0282.
  - [44] J. Andersen et al. (SM and NLO Multileg Working Group), pp. 21–189 (2010), 1003.1241.
  - [45] G. Aad et al. (ATLAS Collaboration), JHEP **1012**, 060 (2010), 1010.2130.
  - [46] S. Chatrchyan et al. (CMS Collaboration), JHEP **1110**, 132 (2011), 1107.4789.
  - [47] G. Watt, JHEP **1109**, 069 (2011), 1106.5788.
  - [48] R. M. Barnett, Phys.Rev.Lett. **36**, 1163 (1976).
  - [49] G. P. Salam and J. Rojo, Comput.Phys.Comm. **180**, 120 (2009), 0804.3755.
  - [50] F. Aaron et al. (H1 Collaboration), Eur.Phys.J. **C71**, 1769 (2011), 1106.1028.
  - [51] J. Pumplin, D. Stump, R. Brock, D. Casey, J. Huston, et al., Phys.Rev. **D65**, 014013 (2001), hep-ph/0101032.
  - [52] D. Stump, J. Pumplin, R. Brock, D. Casey, J. Huston, et al., Phys.Rev. **D65**, 014012 (2001), hep-ph/0101051.
  - [53] P. M. Nadolsky and Z. Sullivan, eConf **C010630**, P510 (2001), hep-ph/0110378.
  - [54] R. A. Fisher, *Statistical methods for research workers* (Oliver and Boyd, Edinburgh, 1925), chap. 4, an Internet version of the 1st edition at <http://psychclassics.yorku.ca/Fisher/Methods/>.
  - [55] T. Lewis, Austral. J. Statist. **30A**, 160 (1988).
  - [56] G. D’Agostini, *Bayesian reasoning in high-energy physics: Principles and applications*, CERN-99-03, CERN-YELLOW-99-03 (1999), sec. 6.3.
  - [57] G. D’Agostini, Nucl.Instrum.Meth. **A346**, 306 (1994).
  - [58] R. D. Ball, S. Carrazza, L. Del Debbio, S. Forte, J. Gao, et al. (2012), 1211.5142.
  - [59] R. D. Ball et al. (NNPDF Collaboration), JHEP **1005**, 075 (2010), 0912.2276.
  - [60] F. Aaron et al. (H1 and ZEUS Collaboration), JHEP **1001**, 109 (2010), 0911.0884.
  - [61] A. Benvenuti et al. (BCDMS Collaboration), Phys.Lett. **B223**, 485 (1989).
  - [62] A. Benvenuti et al. (BCDMS Collaboration), Phys.Lett. **B237**, 592 (1990).
  - [63] M. Arneodo et al. (New Muon Collaboration), Nucl.Phys. **B483**, 3 (1997), hep-ph/9610231.
  - [64] J. Berge, H. Burkhardt, F. Dydak, R. Hagelberg, M. Krasny, et al., Z.Phys. **C49**, 187 (1991).
  - [65] U.-K. Yang et al. (CCFR/NuTeV Collaboration), Phys.Rev.Lett. **86**, 2742 (2001), hep-ex/0009041.
  - [66] W. Seligman, C. Arroyo, L. de Barbaro, P. de Barbaro, A. Bazarko, et al., Phys.Rev.Lett. **79**, 1213 (1997), hep-ex/9701017.
  - [67] D. A. Mason, Ph.D. thesis (2006).
  - [68] M. Goncharov et al., Phys.Rev. **D64**, 112006 (2001), hep-ex/0102049.
  - [69] C. Adloff et al. (H1 Collaboration), Phys.Lett. **B528**, 199 (2002), hep-ex/0108039.
  - [70] A. Aktas et al. (H1 Collaboration), Eur.Phys.J. **C40**, 349 (2005), hep-ex/0411046.
  - [71] A. Aktas et al. (H1 Collaboration), Eur.Phys.J. **C45**, 23 (2006), hep-ex/0507081.
  - [72] J. Breitweg et al. (ZEUS Collaboration), Eur.Phys.J. **C12**, 35 (2000), hep-ex/9908012.
  - [73] S. Chekanov et al. (ZEUS Collaboration), Phys.Rev. **D69**, 012004 (2004), hep-ex/0308068.
  - [74] G. Moreno, C. Brown, W. Cooper, D. Finley, Y. Hsiung, et al., Phys.Rev. **D43**, 2815 (1991).
  - [75] R. Towell et al. (FNAL E866/NuSea Collaboration), Phys.Rev. **D64**, 052002 (2001), hep-ex/0103030.
  - [76] J. Webb et al. (NuSea Collaboration) (2003), hep-ex/0302019.
  - [77] F. Abe et al. (CDF Collaboration), Phys.Rev.Lett. **77**, 2616 (1996).



- [78] D. Acosta et al. (CDF Collaboration), Phys.Rev. **D71**, 051104 (2005), hep-ex/0501023.
- [79] V. Abazov et al. (D0 Collaboration), Phys.Rev.Lett. **101**, 211801 (2008), 0807.3367.
- [80] V. Abazov et al. (D0 Collaboration), Phys.Rev. **D77**, 011106 (2008), 0709.4254.
- [81] V. Abazov et al. (D0 Collaboration), Phys.Lett. **B658**, 112 (2008), hep-ex/0608052.
- [82] T. A. Aaltonen et al. (CDF Collaboration), Phys.Lett. **B692**, 232 (2010), 0908.3914.
- [83] T. Aaltonen et al. (CDF Collaboration), Phys.Rev. **D78**, 052006 (2008), 0807.2204.
- [84] V. Abazov et al. (D0 Collaboration), Phys.Rev.Lett. **101**, 062001 (2008), 0802.2400.
- [85] S. D. Ellis, Z. Kunszt, and D. E. Soper, Phys.Rev.Lett. **69**, 1496 (1992).
- [86] J. Gao, Z. Liang, D. E. Soper, H.-L. Lai, P. M. Nadolsky, et al. (2012), 1207.0513.
- [87] Z. Nagy, Phys.Rev. **D68**, 094002 (2003), hep-ph/0307268.
- [88] T. Kluge, K. Rabbertz, and M. Wobisch (2006), hep-ph/0609285.
- [89] <http://projects.hepforge.org/fastnlo/form/index.html>.
- [90] M. Wobisch, D. Britzger, T. Kluge, K. Rabbertz, and F. Stober (FastNLO Collaboration) (2011), 1109.1310.
- [91] T. Carli, D. Clements, A. Cooper-Sarkar, C. Gwenlan, G. P. Salam, et al., Eur.Phys.J. **C66**, 503 (2010), 0911.2985.
- [92] N. Kidonakis and J. Owens, Phys.Rev. **D63**, 054019 (2001), hep-ph/0007268.
- [93] R. Gavin, Y. Li, F. Petriello, and S. Quackenbush, Comput.Phys.Commun. **182**, 2388 (2011), 1011.3540.
- [94] R. Gavin, Y. Li, F. Petriello, and S. Quackenbush (2012), 1201.5896.
- [95] C. Balazs and C.-P. Yuan, Phys.Rev. **D56**, 5558 (1997), hep-ph/9704258.
- [96] F. Landry, R. Brock, P. M. Nadolsky, and C.-P. Yuan, Phys.Rev. **D67**, 073016 (2003), hep-ph/0212159.
- [97] M. Guzzi and P. M. Nadolsky (2012), 1209.1252.
- [98] P. B. Arnold and M. H. Reno, Nucl.Phys. **B319**, 37 (1989).
- [99] P. B. Arnold, R. K. Ellis, and M. Reno, Phys.Rev. **D40**, 912 (1989).
- [100] R. Hamberg, W. van Neerven, and T. Matsuura, Nucl.Phys. **B359**, 343 (1991).
- [101] A. Cafarella, C. Coriano, and M. Guzzi, JHEP **0708**, 030 (2007), hep-ph/0702244.
- [102] A. Cafarella, C. Coriano, and M. Guzzi, Comput.Phys.Commun. **179**, 665 (2008), 0803.0462.
- [103] M. Czakon and A. Mitov (2011), 1112.5675.
- [104] J. Beringer et al. (Particle Data Group), Phys.Rev. **D86**, 010001 (2012).
- [105] M. Cacciari, M. Czakon, M. Mangano, A. Mitov, and P. Nason, Phys.Lett. **B710**, 612 (2012), 1111.5869.
- [106] P. Baernreuther, M. Czakon, and A. Mitov, Phys.Rev.Lett. **109**, 132001 (2012), 1204.5201.
- [107] S. Catani and M. Grazzini, Phys.Rev.Lett. **98**, 222002 (2007), hep-ph/0703012.
- [108] M. Grazzini, JHEP **0802**, 043 (2008), 0801.3232.
- [109] S. Dittmaier et al. (LHC Higgs Cross Section Working Group) (2011), 1101.0593.
- [110] R. V. Harlander and W. B. Kilgore, Phys.Rev. **D68**, 013001 (2003), hep-ph/0304035.
- [111] G. Aad et al. (ATLAS Collaboration), Phys.Rev. **D85**, 072004 (2012), 1109.5141.
- [112] CMS Collaboration, CMS-PAS-SMP-12-011.
- [113] The Tevatron Electroweak Working Group, DØ note 6363, [http://tevewwg.fnal.gov/top/tev\\_ttbarxsec\\_summary.pdf](http://tevewwg.fnal.gov/top/tev_ttbarxsec_summary.pdf).
- [114] ATLAS Collaboration, ATLAS-CONF-2012-024, ATLAS-COM-CONF-2012-009.
- [115] G. Aad et al. (ATLAS Collaboration), Phys.Lett. **B717**, 89 (2012), 1205.2067.
- [116] ATLAS Collaboration, ATLAS-CONF-2012-131, ATLAS-COM-CONF-2012-056.
- [117] G. Aad et al. (ATLAS Collaboration) (2012), 1211.7205.

- [118] ATLAS Collaboration, ATLAS-CONF-2012-149.
- [119] S. Chatrchyan et al. (CMS Collaboration) (2012), 1212.6682.
- [120] S. Chatrchyan et al. (CMS Collaboration), Phys.Rev.Lett. **109**, 111806 (2012), 1206.2598.
- [121] R. Aaij et al. (LHC-B Collaboration), JHEP **1206**, 058 (2012), 1204.1620.
- [122] K. Melnikov and F. Petriello, Phys.Rev. **D74**, 114017 (2006), hep-ph/0609070.
- [123] S. Catani, L. Cieri, G. Ferrera, D. de Florian, and M. Grazzini, Phys.Rev.Lett. **103**, 082001 (2009), 0903.2120.
- [124] M. Guzzi, P. Nadolsky, E. Berger, H.-L. Lai, F. Olness, et al. (2011), 1101.0561.
- [125] G. Aad et al. (ATLAS Collaboration), Phys.Rev.Lett. **109**, 012001 (2012), 1203.4051.